

Silicon quantum processor with robust long-distance qubit couplings

Guilherme Tosi,¹ Fahd A. Mohiyaddin,¹ Vivien Schmitt,¹ Stefanie Tenberg,¹ Rajib Rahman,² Gerhard Klimeck,² and Andrea Morello¹

¹*Centre for Quantum Computation and Communication Technology,
School of Electrical Engineering & Telecommunications,
UNSW Sydney, New South Wales 2052, Australia.*

²*Network for Computational Nanotechnology, Purdue University, West Lafayette, Indiana 47907, United States*
(Dated: March 10, 2017)

Practical quantum computers require the construction of a large network of highly coherent qubits, interconnected in a design robust against errors. Donor spins in silicon provide state-of-the-art coherence and quantum gate fidelities, in a physical platform adapted from industrial semiconductor processing. Here we present a scalable design for a silicon quantum processor that does not require precise donor placement and allows hundreds of nanometers inter-qubit distances, therefore facilitating fabrication using current technology. All qubit operations are performed via electrical means on the electron-nuclear spin states of a phosphorus donor. Single-qubit gates use low power electric drive at microwave frequencies, while fast two-qubit gates exploit electric dipole-dipole interactions. Microwave resonators allow for millimeter-distance entanglement and interfacing with photonic links. Sweet spots protect the qubits from charge noise up to second order, implying that all operations can be performed with error rates below quantum error correction thresholds, even without any active noise cancellation technique.

The successful implementation of quantum algorithms requires incorporation of error correction codes¹ that deal with the fragile nature of qubits. The highest tolerances in error rates are found when using nearest-neighbor topological codes², long-distance entanglement links³ or a combination of both⁴. There exist several physical platforms where state preservation⁵⁻⁷, qubit control⁸⁻¹¹ and 2-qubit logic gates^{8,12} are achieved with fault-tolerant fidelities. The ultimate goal is to integrate a large number of qubits in expandable arrays to construct a scalable, universal quantum processor.

Donor spin qubits in silicon are an appealing physical platform for that goal, due to their integrability with Metal-Oxide-Semiconductor (MOS) structure and nanometric unit size¹³. By using isotopically enriched ²⁸Si as the substrate material¹⁴, donor spins offer coherence times around a minute⁷ or an hour⁶, and control error rates as small as 10^{-4} (ref. 11). However, integrating several of these qubits in a scalable architecture remains a formidable challenge, mainly because of the difficulty in achieving reliable 2-qubit gates.

The seminal Kane proposal¹⁵ for a nuclear-spin quantum computer in silicon described the use of short-range

exchange interactions J between donor-bound electrons, to mediate an effective inter-nuclear coupling of order ~ 100 kHz at a ~ 15 nm distance. However, the exchange interaction has an exponential and oscillatory spatial behavior that can result in an order of magnitude variation in strength upon displacement by a single lattice site^{16,17}. Notwithstanding, plenty of progress has been made in the experimental demonstration of the building blocks of a Kane-type processor¹⁸⁻²¹, including the observation of inter-donor exchange²²⁻²⁴. Slightly relaxed requirements on donor placement can be found when using a hyperfine-controlled exchange interaction between electron spin qubits²⁵, or a slower magnetic dipole-dipole coupling effective at ~ 30 nm distances²⁶. Other proposals space donors further apart by introducing some intermediate coupler, *e.g.* donor chains^{27,28}, charge-coupled devices²⁹, ferromagnets³⁰, probe spins³¹ or quantum dots³².

Here we introduce the design of a large-scale, donor-based silicon quantum processor based upon electric dipole interactions. This processor could be fabricated using existing technology, since it does not require precise donor placement. The large inter-qubit spacing, > 150 nm, leaves sufficient space to intersperse classical control and readout devices, while retaining some of the compactness of atomic-size qubits. New stabilization schemes largely decouple the qubits from electric noise while still keeping them sensitive to electric drive and mutual coupling. Finally, the whole structure retains the standard silicon MOS materials stack, important for ultimate manufacturability.

Coupling Si:P spin qubits to electric fields

The phosphorus donor in silicon comprises an electron spin $S = 1/2$ with gyromagnetic ratio $\gamma_e = 27.97$ GHz/T and basis states $|\downarrow\rangle, |\uparrow\rangle$, and a nuclear spin $I = 1/2$ with gyromagnetic ratio $\gamma_n = 17.23$ MHz/T and basis states $|\downarrow\rangle, |\uparrow\rangle$. The electron interacts with the nucleus through the hyperfine coupling $A \approx 117$ MHz. When placed in a large magnetic field B_0 ($\gamma_+ B_0 \gg A$, with $\gamma_+ = \gamma_e + \gamma_n$), the eigenstates of the system are the separable tensor products of the basis states, *i.e.* $|\downarrow\uparrow\rangle, |\downarrow\downarrow\rangle, |\uparrow\downarrow\rangle, |\uparrow\uparrow\rangle$ (Fig. 1c). The electron and the nucleus can be operated as single qubits by applying oscillating magnetic fields resonant with any of the transitions frequencies between eigenstates that differ by the flipping of one of the spins, *e.g.* $|\downarrow\uparrow\rangle \leftrightarrow |\uparrow\uparrow\rangle$ for the electron qubit, etc (Fig. 1c).

We envisage a device where a shallow ³¹P donor is em-

bedded in an isotopically pure ^{28}Si crystal at a depth z_d from the interface with a thin SiO_2 layer (Fig. 1a). The orbital wavefunction ψ of the donor-bound electron can be controlled by a vertical electric field E_z applied by a metal gate on top. It changes from a bulk-like donor state at low electric fields to an interface-like state at high-fields^{33,34} (insets in Fig. 1d). The hyperfine interaction $A(E_z)$, proportional to the square amplitude of the electron wavefunction at the donor site $|\psi(0, 0, z_d)|^2$, changes accordingly from the bulk value $A \approx 117$ MHz to $A \approx 0$ when the electron is fully displaced to the interface (Fig. 1d). Shifting the electron wavefunction also results in the creation of an electric dipole $\mu_e = ed$, where e is the electron charge and d is the separation between the mean positions of the donor-bound and interface-bound wavefunctions ($d \lesssim z_d$, see Supplementary Information S1). The induced electric dipole μ_e has been largely overlooked in the past, but plays a crucial role in this proposal.

The key idea is to define a new qubit, called henceforth the *flip-flop qubit*, described in the subspace spanned by the states $|\downarrow\uparrow\rangle, |\uparrow\downarrow\rangle$. Transitions between these basis states cannot be induced by magnetic resonance, because there is no change in the z -component of the total angular momentum. However, the hyperfine interaction, $\mathbf{AS} \cdot \mathbf{I}$, is a transverse term in the flip-flop basis, since its eigenstates are $S = (|\downarrow\uparrow\rangle - |\uparrow\downarrow\rangle)/\sqrt{2}$, $T_0 = (|\downarrow\uparrow\rangle + |\uparrow\downarrow\rangle)/\sqrt{2}$ (Fig. 1b). Therefore, electrically modulating $A(E_z)$ at the frequency

$$\epsilon_{\text{ff}}(A) = \sqrt{(\gamma_+ B_0)^2 + [A(E_z)]^2}, \quad (1)$$

corresponding to the flip-flop qubit energy splitting, causes an electric dipole spin resonance (EDSR) transition between the $|\downarrow\uparrow\rangle, |\uparrow\downarrow\rangle$ basis states^{35,36} (Fig. 1c). This transition is faster at the ‘‘ionization point’’, where the electron is shared halfway between donor and interface, since $A(E_z)$ can vary strongly upon the application of a small voltage on the top gate.

Electrical noise and relaxation

Since the qubit operation is based upon the use of electric fields, a natural concern is the fragility of the qubit states in the presence of electric noise. Below we show that there are special bias points that render the flip-flop qubit operation highly robust against noise.

A quantum-mechanical description of the system is obtained by treating also the electron position as a two-level system (effectively a charge qubit; see Supplementary Information S1 for a justification of this two-level approximation), where the vertical position of the electron is represented by a Pauli σ_z operator, with eigenvectors $|d\rangle$, for the electron at the donor, and $|i\rangle$ at the interface (Fig. 1a,d). The simplified orbital Hamiltonian reads (in units of Hz):

$$\mathcal{H}_{\text{orb}} = \frac{V_t \sigma_x - [e(E_z - E_z^0)d/h] \sigma_z}{2}, \quad (2)$$

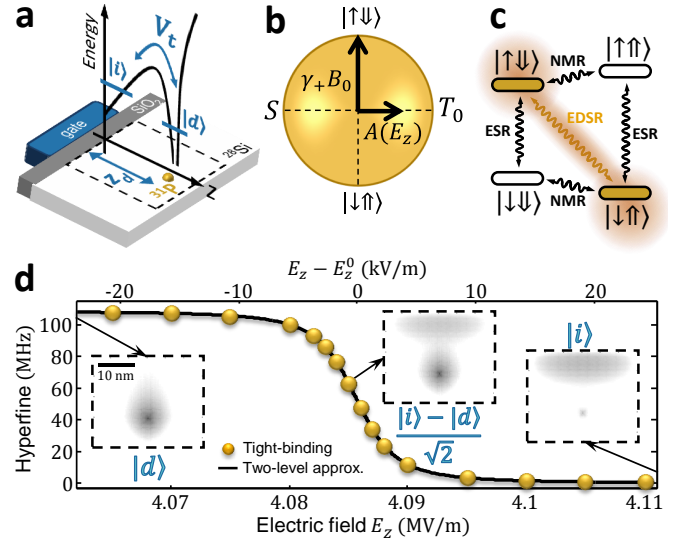


FIG. 1. **Coupling Si:P spin qubits to electric fields via hyperfine modulation.**

a, Qubit unit cell, in which the electron interface state, $|i\rangle$, is coupled to the donor-bound state, $|d\rangle$, by a tunnel rate V_t . Plot shows conduction band profile along z . **b**, Bloch sphere of a flip-flop spin qubit coupled to a vertical electric field E_z via the hyperfine interaction A . Singlet and triplet states are denoted by $S = (|\downarrow\uparrow\rangle - |\uparrow\downarrow\rangle)/\sqrt{2}$ and $T_0 = (|\downarrow\uparrow\rangle + |\uparrow\downarrow\rangle)/\sqrt{2}$. **c**, Si:P electron-nuclear spin levels, showing standard electron spin resonance (ESR) and nuclear magnetic resonance (NMR) transitions, together with hyperfine-enabled EDSR. **d**, Atomistic tight-binding simulations³⁷ (dots) of the electron-nucleus hyperfine interaction, for a $z_d = 15.2$ nm deep donor, as a function of vertical electric field. The solid line is a fit using the simplified two-level Hamiltonian $\mathcal{H}_{\text{orb}} + \mathcal{H}_A^{\text{orb}}$, which yields $V_t = 9.3$ GHz (see Supplementary Information S1). Insets show the electron ground-state, $|g\rangle$, wavefunction, in the region within dashed lines in **a**, for three different vertical electric fields.

where V_t is the tunnel coupling between the donor and the interface potential wells, E_z^0 is the vertical electric field at the ionization point and h is the Planck constant. The electron ground $|g\rangle$ and excited $|e\rangle$ orbital eigenstates depend on E_z (Fig. 1d) and have an energy difference given by:

$$\epsilon_o = \sqrt{(V_t)^2 + [e(E_z - E_z^0)d/h]^2} \quad (3)$$

At the ionization point, the energy difference between eigenstates $|e\rangle = (|d\rangle + |i\rangle)/\sqrt{2}$ and $|g\rangle = (|d\rangle - |i\rangle)/\sqrt{2}$ is minimum and equal to V_t (Fig. 2a), and therefore first-order insensitive to electric noise, $\partial\epsilon_o/\partial E_z = 0$. This bias point is referred to as the ‘‘charge qubit sweet spot’’³⁸ (CQSS – Fig. 2a).

Conversely, the bare flip-flop qubit energy is expected to depend strongly on E_z , through the combined effect of the hyperfine interaction A (Eq. 1) and the orbital dependence of the electron gyromagnetic ratio, γ_e . Indeed, the gyromagnetic ratio of an electron confined at a

Si/SiO₂ interface can differ from that of a donor-bound electron by a relative amount Δ_γ up to 0.7%³⁹. Therefore, the Zeeman terms in the Hamiltonian must include a dependence of the electron Zeeman splitting on its orbital position, i.e. the charge qubit σ_z operator:

$$\mathcal{H}_{B_0}^{\text{orb}} = \gamma_e B_0 \left[1 + \left(\frac{1 + \sigma_z}{2} \right) \Delta_\gamma \right] S_z - \gamma_n B_0 I_z. \quad (4)$$

We can also write the hyperfine coupling as an operator that depends on the charge qubit state:

$$\mathcal{H}_A^{\text{orb}} = A \left(\frac{1 - \sigma_z}{2} \right) \mathbf{S} \cdot \mathbf{I} \quad (5)$$

Indeed, this simple two-level approximation, shown as a black line in Fig 1d, reproduces the full tight-binding simulations (yellow dots).

The overall flip-flop qubit transition frequency as a function of E_z becomes:

$$\epsilon_{\text{ff}}(A, \gamma_e) = \sqrt{[\gamma_e(E_z) + \gamma_n]^2 B_0^2 + [A(E_z)]^2}, \quad (6)$$

shown in Fig. 2a (dashed line), where we assumed $\Delta_\gamma = -0.2\%$ ³⁹. $\epsilon_{\text{ff}}(A, \gamma_e)$ shows a steep slope around the ionization point, mostly caused by the E_z -dependence of γ_e (the dependence on A is less significant because $\gamma_+ B_0 \gg A$). Therefore, while $E_z \approx E_z^0$ is the fastest operation point for the flip-flop qubit driven by a resonant modulation of A , it can also be the most prone to qubit dephasing from charge and gate noise, through the influence of E_z on γ_e .

However, computing instead the *full* flip-flop qubit Hamiltonian,

$$\mathcal{H}_{\text{ff}} = \mathcal{H}_{B_0}^{\text{orb}} + \mathcal{H}_A^{\text{orb}} + \mathcal{H}_{\text{orb}}, \quad (7)$$

reveals that the qubit transition frequency has an extra bend around the ionization point (Fig. 2a – thick yellow line). This comes from Eq. 5, which provides a transverse coupling g_{so} between the flip-flop and charge qubits (inset in Fig. 2a):

$$g_{\text{so}} = \frac{A V_t}{4 \epsilon_o} \quad (8)$$

As a result, the electron orbit dispersively shifts the flip-flop qubit by, to second order:

$$D_{\text{orb}}(E_z) = \frac{[g_{\text{so}}(E_z)]^2}{\delta_{\text{so}}(E_z)}, \quad (9)$$

where $\delta_{\text{so}} = \epsilon_o - \epsilon_{\text{ff}}$, reducing the flip-flop qubit frequency to:

$$\epsilon_{\text{ff}}(A, \gamma_e, D_{\text{orb}}) = \epsilon_{\text{ff}}(A, \gamma_e) - D_{\text{orb}}(E_z), \quad (10)$$

$D_{\text{orb}}(E_z)$ is largest around $E_z \approx E_z^0$, since δ_{so} is lowest (i.e. the charge qubit frequency comes closest to the flip-flop qubit, Fig. 2a) and g_{so} is highest. Eq. 10 (thin black line in Fig. 2a) agrees with full numerical simulations of the Hamiltonian in Eq. 7.

Such a dispersive shift stabilizes the flip-flop precession frequency against noise. To quantify that, we assume a quasi-static electric field noise with 100 V/m r.m.s. amplitude along the donor-dot direction (z -axis in Fig. 1a). This noise is equivalent to a 1.5 μeV charge detuning noise for $d = 15$ nm, consistent with measured values^{40–42} – see Supplementary Information S3. The estimated – see Methods section – dephasing rates can be as low as $1/T_2^* \approx 3$ kHz (Fig. 2b), comparable to the ones due to magnetic noise ($1/T_2^* \approx 1$ kHz in ²⁸Si nanostructures⁷). This can be understood from Fig. 2c, which shows the qubit precession frequency dependence on E_z , for three different values of V_t . For small detunings δ_{so} , i.e. V_t close to ϵ_{ff} , the dispersive shift around the ionization point is strong, yielding two first-order “clock transitions” (CT), where $\partial\epsilon_{\text{ff}}/\partial E_z = 0$ where the dephasing rate is reduced. By increasing V_t , the two first-order points merge into a single one in which both the first and second derivatives vanish, yielding the slowest qubit dephasing.

Another source of errors could come from relaxation via coupling to phonons. This is not an issue for bulk donors, where electron spin relaxation time is $T_{1,s} \gg 1$ s¹⁸. However, due to the particular valley composition of the flip-flop qubit near the ionization point, its relaxation rate $1/T_{1,\text{ff}}$ due to charge-phonon coupling is enhanced⁴³. We estimate it by noting that, if $\delta_{\text{so}} \gg g_{\text{so}}$, $1/T_{1,\text{ff}}$ is equal to the amount of charge excited state in the flip-flop eigenstates⁴⁴ times the charge relaxation rate⁴³:

$$1/T_{1,\text{ff}} = (g_{\text{so}}/\delta_{\text{so}})^2 / T_{1,o}, \quad (11a)$$

$$1/T_{1,o} = \Theta \epsilon_o V_t^2, \quad (11b)$$

where $T_{1,o}$ is the charge qubit lifetime and $\Theta \approx 2.37 \times 10^{-24} \text{ s}^2$ is determined by the silicon crystal properties⁴³. Therefore, as can be seen from Fig. 2d, the higher the detuning δ_{so} , the slower the relaxation. In particular, at the 2nd-order CT, the qubit dephasing can be limited by relaxation, $1/T_2^* = 1/2T_1 \approx 10^4$ Hz. This limitation can be overcome by reducing B_0 (Fig. 2e).

Tuning a flip-flop qubit at a clock transition requires the ability to tune the tunnel coupling V_t . The latter is difficult to control at the fabrication stage, given its exponential dependence on donor depth, together with oscillations at the atomic scale⁴⁵ arising from a similar valley interference effect as the one afflicting the exchange interaction¹⁶. To overcome that, V_t can be electrostatically tuned, by at least 2 orders of magnitude, by using

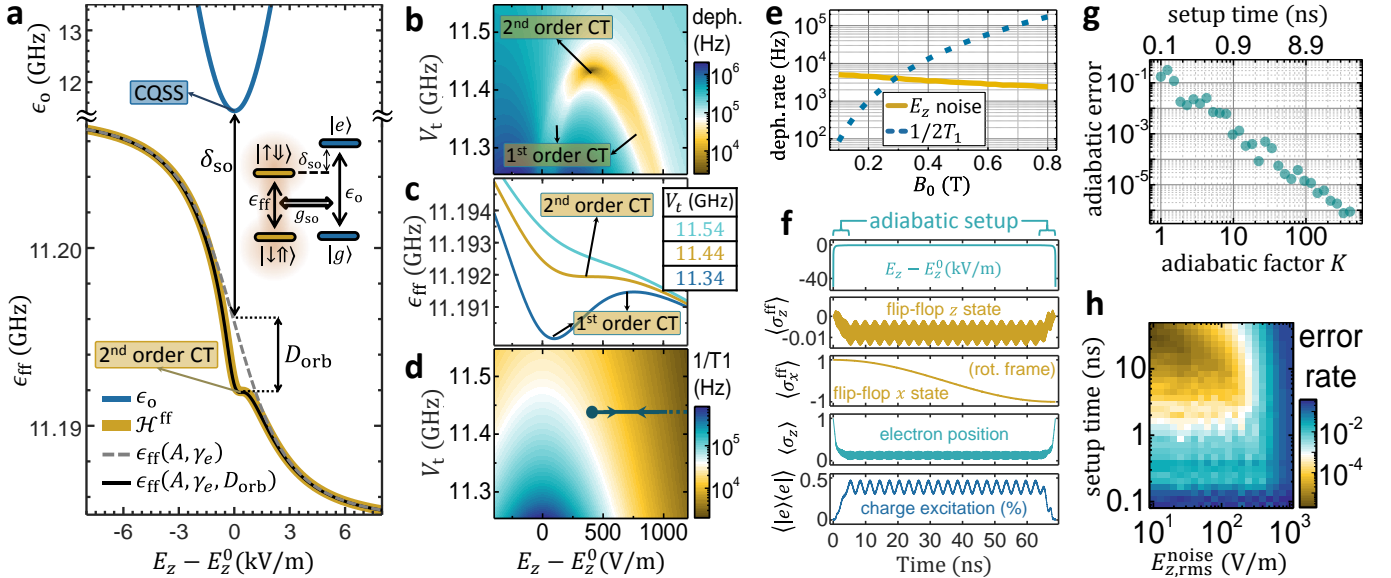


FIG. 2. **Robustness to electric noise and high-fidelity adiabatic z -gates.** **a**, Charge, ϵ_0 , and flip-flop, ϵ_{ff} , qubits transition frequencies as a function of vertical electric field E_z , for $B_0 = 0.4$ T, $A = 117$ MHz, $d = 15$ nm, $\Delta_\gamma = -0.2\%$ and $V_t = 11.44$ GHz. Inset shows the level diagram of flip-flop states coupled to charge states. CT stands for “clock transition” and CQSS for “charge qubit sweet spot”. **b**, Estimated flip-flop qubit dephasing rate, assuming electric field noise $E_{z,\text{rms}}^{\text{noise}} = 100$ V/m. **c**, E_z -dependence of flip-flop precession frequency for the three indicated tunnel coupling values, with arrows indicating adiabatic path used for z -gates. **d**, Flip-flop qubit relaxation rate, at 2nd-order CTs for each B_0 . **e**, Flip-flop qubit dephasing rate due to E_z noise and relaxation, at 2nd-order CTs for each B_0 . **f**, Time-evolution of an adiabatic ($K = 50$) π z -gate on state $|g\rangle \otimes (|\downarrow\uparrow\rangle + |\uparrow\downarrow\rangle)/\sqrt{2}$, showing applied electric field and flip-flop/charge states. Outer brackets denote the expected value of an operator. $\sigma_z^{\text{ff}} = |\uparrow\downarrow\rangle\langle\uparrow\downarrow| - |\downarrow\uparrow\rangle\langle\downarrow\uparrow|$ and $\sigma_x^{\text{ff}} = |+\frac{\text{ff}}{x}\rangle\langle+\frac{\text{ff}}{x}| - |-\frac{\text{ff}}{x}\rangle\langle-\frac{\text{ff}}{x}|$, where $|+\frac{\text{ff}}{x}\rangle = (|\uparrow\downarrow\rangle + \exp(-i2\pi\epsilon_{\text{ff}}^{t=0})|\downarrow\uparrow\rangle)/\sqrt{2}$ and $|-\frac{\text{ff}}{x}\rangle = (|\uparrow\downarrow\rangle + \exp(-i2\pi\epsilon_{\text{ff}}^{t=0} - i\pi)|\downarrow\uparrow\rangle)/\sqrt{2}$. Fast oscillations between the charge and flip-flop states are due to small deviations from perfect adiabaticity. **g**, π z -gate leakage error for different adiabatic setup times, which are set by the factor K . **h**, π z -gate error due to quasi-static E_z noise, at the 2nd-order CT at $B_0 = 0.4$ T, for different noise amplitudes and adiabatic setup times.

a gate stack identical to the well-established scheme for the confinement of single electrons in Si quantum dots¹⁰ – see Supplementary Information S2.

The presence of slow dephasing regions is important to control the qubit phase with high fidelity. In our quantum processor, idle qubits are decoupled from electric fields by fully displacing the electron either to the interface or to the donor. Performing quantum operations on the qubit requires displacing the electrons close to the ionization point, which in turn changes its precession frequency (Fig. 2a). As a result, the accumulated phase must be corrected after quantum operations. This is optimally done by moving the electron to the 2nd-order clock transition, therefore minimizing dephasing errors. At this point, the flip-flop qubit phase precesses $\sim \Delta_\gamma \gamma_e B_0 / 2 - D_{\text{orb}}$ faster than its idle point, and therefore any phase correction in a 2π period can be applied within tens of ns. The dephasing rate at the CT, on the order of a few kHz, would cause very small errors ($< 10^{-4}$). However, while moving the electron from the interface towards the donor, the flip-flop qubit goes through regions of fast dephasing (Fig. 2b), and therefore this operation has to be performed as quickly as possible. It also has to be slow enough as to avoid errors due to

non-adiabaticity, which include *e.g.* leakage to unwanted high-energy states. These errors depend on the adiabatic factor K , which quantifies the fractional rate of change of the system’s eigenstates (the higher the value of K , the more adiabatic and slower is the process – see Methods).

In Fig. 2f we plot the time dynamics of an initial state $|g\rangle \otimes (|\downarrow\uparrow\rangle + |\uparrow\downarrow\rangle)/\sqrt{2}$ while sweeping E_z adiabatically ($K = 50$) to move the electron from the interface to the 2nd-order CT and back, in order to realize a π z -gate. The initial adiabatic setup part consists of a fast sweep (0.8 ns), allowed by the large charge qubit splitting when $E_z \gg E_z^0$, followed by a slower sweep (3.5 ns), limited by the proximity of excited charge states to the flip-flop qubit when $E_z \approx E_z^0$. The electron then remains at the CT for 60 ns, before adiabatically moving back to the interface. During the total 69 ns, the flip-flop qubit phase is shifted by π , with adiabatic errors, averaged over a set of initial flip-flop states – see Methods – around 10^{-4} . These errors can be controlled with the factor K , which sets the setup time (see Fig. 2g).

Quasi-static E_z noise increases errors, due to dephasing (Fig. 2h). At realistic noise levels (100 V/m), the gate error rate is found to be $< 10^{-4}$. Similar error levels arise due to relaxation, which remains below 3×10^4 Hz

(Fig. 2d).

Note that the presence of clock transitions does not affect the ability to use E_{ac} to resonantly drive the qubit, since the transverse term $A(E_z)$ still responds fully to the electric field (this is similar to the case of magnetic clock transitions, e.g. in Si:Bi⁴⁶).

Electric drive of flip-flop qubit

We now explain how high-fidelity 1-qubit $x(y)$ -gates can be achieved via electric drive of the flip-flop qubit. The fastest 1-qubit gates are obtained when the electron is around the ionization point, where $\partial A/\partial E_z$ is maximum (Fig. 1d). A vertical oscillating electric field of amplitude E_{ac} is applied (Fig. 3a) in resonance with the flip-flop qubit, *i.e.*, $\nu_E = \epsilon_{ff}$. A large detuning $\delta_{so} \gg g_{so}$ ensures the least amount of the charge excited state $|e\rangle$ in the qubit eigenstates, minimizing qubit relaxation via charge-phonon coupling. The flip-flop qubit is still driven, via a second-order process, at a rate (half-Rabi frequency):

$$g_E^{ff} = \frac{g_{so}g_E}{2} \left(\frac{1}{\delta_{so}} + \frac{1}{\delta_E} \right), \quad (12)$$

where $\delta_E = \nu_E - \epsilon_o$ and g_E is the driven electric coupling rate between the two charge eigenstates:

$$g_E = \frac{eE_{ac}d V_t}{4h \epsilon_o}, \quad (13)$$

where E_{ac} is the amplitude of a sinusoidal drive. Equation 12 provides another explanation why the fastest 1-qubit gates are obtained when the electron is at the ionization point: δ_{so} and δ_E are minimum (ϵ_o is minimum), and g_{so} and g_E are maximum (Eqs. 8 and 13).

The electrical drive can cause some excitation of the charge qubit. It is therefore convenient to turn E_{ac} on/off adiabatically to make sure the charge is de-excited at the end of the gate. Figure 3c shows the E_{ac} time evolution needed for a $\pi/2$ x -gate, where we have assumed an adiabatic factor $K = 30$, sufficient for leakage errors $< 10^{-3}$. E_{ac} increases steadily until a $\pi/4$ rotation is completed, after which E_{ac} is gradually switched off to achieve an adiabatic $\pi/2$ x -gate. An average 4% excitation of the charge qubit causes a $\sim 4 \times 10^4$ Hz relaxation rate of the encoded quantum state (Eq. 11b), or error levels close to 10^{-3} .

We then investigate how the total $\pi/2$ x -gate errors depend on the biasing of the electron wavefunction. At the ionization point, $E_z = E_z^0$, error levels close to 10^{-3} are found over a wide range of V_t (Fig. 3e). The $K = 30$ choice ensures adiabatic errors $< 10^{-3}$ with an oscillatory character typical of adiabatic processes⁴⁷. At small V_t (and therefore small detuning δ_{so}), the qubit eigenstates contain a substantial amount of charge, causing more errors due to charge-phonon relaxation. Increasing the detuning δ_E with larger V_t allows for a faster adiabatic sweep and higher powers (Fig. 3d), yielding shorter

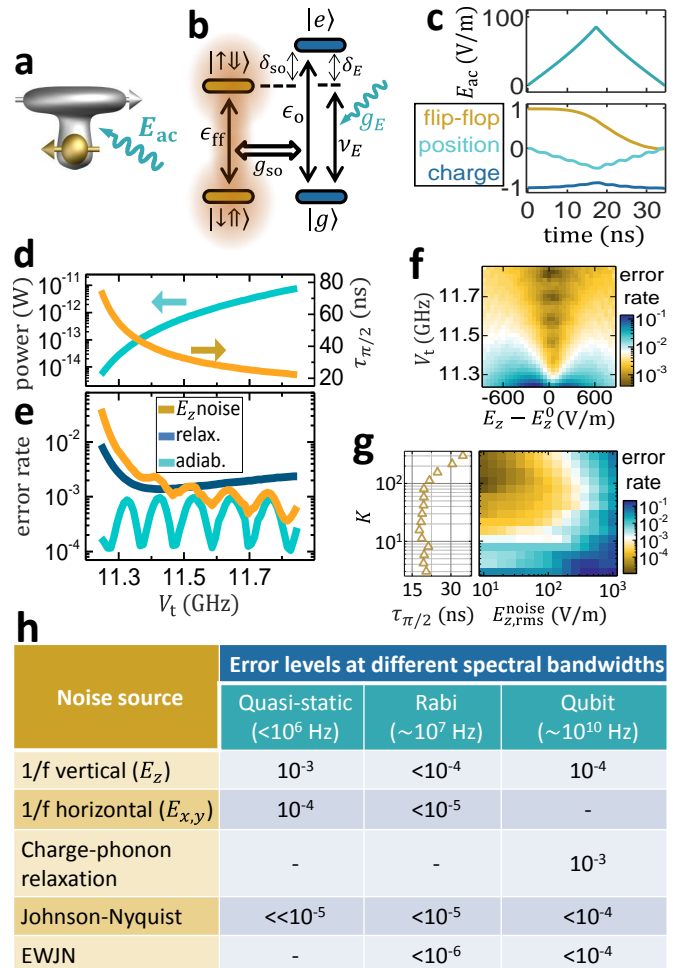


FIG. 3. High-fidelity electrically-driven adiabatic 1-qubit $x(y)$ -gates. **a**, Spatial representation and **b**, level diagram, for electrical drive of a flip-flop qubit, showing partially ionized electron wavefunction and spin arrows. **c**, Time-dependent adiabatic drive amplitude and qubit dynamics of a $\pi/2$ x -gate, for $K = 30$, $B_0 = 0.4$ T, $E_z = E_z^0$ and $V_t = 11.5$ GHz. Bottom plot shows flip-flop z state, $\langle \sigma_z^{\text{ff}} \rangle$, electron position, $\langle \sigma_z \rangle$, and charge qubit state, $\langle |e\rangle \langle e| - |g\rangle \langle g| \rangle$. For the same parameters, **d** shows the averaged drive power and gate time, and **e** the error rates for different V_t . To estimate the drive power, we assumed a 50 Ω line in which a 1 μV AC voltage produces a 10 V/m AC vertical electric field. **f**, Estimated flip-flop qubit $\pi/2$ x -gate error due to quasi-static noise with amplitude $E_{z,rms}^{\text{noise}} = 100$ V/m. **g**, Dependence of gate error rate on the electric noise r.m.s. amplitude and adiabatic factor K (which sets the gate time). **h**, Estimated gate error rates from different noise sources, according to Supplementary Information S3. Hyphens indicate inexistent/negligible errors.

gate times and therefore less errors due to quasi-static noise. Still, the incident power is at least three orders of magnitude lower than the one needed to drive donor electron spin qubits, at the same Rabi frequency, with oscillating magnetic fields^{7,19}.

As Fig. 3f shows, low error rates are still available

away from the ionization point, even though best values are found at $E_z = E_z^0$. This is because our gate times are so fast that dephasing, and therefore CT's, do not play a crucial role. Instead, quasi-static E_z noise cause errors mainly by modulating the driving strength g_E^{ff} , causing "gate time jitter". Indeed, the gate time is sensitive to the orbital transition frequency ϵ_o (Eq. 12), and therefore gate errors are minimized close to the charge qubit sweet spot (CQSS), where $\partial\epsilon_o/\partial E_z = 0$ (Fig. 2a).

Finally, as Fig. 3g shows, lower quasi-static E_z noise can cause less errors, provided that the adiabatic factor K is increased, to reduce leakage errors, up to an optimum value where gate times are still fast as to keep noise errors low. Relaxation errors could also be reduced by reducing B_0 (recall Fig. 2e).

A number of other noise sources, including high frequency charge noise, Johnson-Nyquist and evanescent-wave Johnson noise⁴⁸ (EWJN) also affect qubits that are sensitive to electric fields. However, as we discuss in Supplementary Information S3, the corresponding error rates are much lower than the ones already previously mentioned – see all estimated error levels in Fig. 3h.

Two-qubit coupling via electric dipole interaction

We now present the new method to couple donor spins that lies at the heart of our scalable quantum processor. It exploits the electric dipole that naturally arises when a donor-electron wavefunction is biased to the ionization point (Fig. 4a), due to the fact that a negative charge has been partly displaced away from the positive ³¹P nucleus. The electric field produced by this induced dipole can, in turn, introduce a coupling term in a nearby donor which is also biased at the ionization point.

The interaction energy between two distant dipoles, μ_1 and μ_2 , oriented perpendicularly to their separation, r , is⁴⁹ $V_{\text{dip}} = \mu_1\mu_2/(4\pi\epsilon_r\epsilon_0r^3)$, where ϵ_0 is the vacuum permittivity and ϵ_r the material's dielectric constant ($\epsilon_r = 11.7$ in silicon). The electric dipole of each donor-interface state is $\mu_i = ed_i(1 + \sigma_{z,i})/2$, implying that the dipole-dipole interaction Hamiltonian is:

$$\mathcal{H}_{\text{dip}} = V_{\text{dd}}(\sigma_{z,1}\sigma_{z,2} + \sigma_{z,1} + \sigma_{z,2}) \quad (14a)$$

$$V_{\text{dd}} = \frac{1}{16\pi\epsilon_0\epsilon_r h} \frac{ed_1 ed_2}{r^3} \quad (14b)$$

This electric dipole-dipole interaction is therefore equivalent to a small shift in the equilibrium orbital position of both electrons plus a coupling term between the charge qubits (blue dashed rectangle in Fig. 4b) equal to:

$$g_{\text{dd}} = V_{\text{dd}} \frac{V_{t,1}V_{t,2}}{\epsilon_{o,1}\epsilon_{o,2}} \quad (15)$$

Most importantly, since each flip-flop qubit is coupled to their electron position (Eq. 5), the electric dipole-dipole interaction provides a natural way to couple two distant flip-flop qubits.

Indeed, the effective coupling rate between two flip-flop qubits at the ionization point, Fig. 4e, exceeds 10^7 Hz around two narrow regions. These bands can be understood from the energy-level diagram shown in Fig. 4c. The two charge qubits in Fig. 4b form hybridized molecular states, which are coupled to each flip-flop qubit. The 2-qubit coupling rate is maximum when in resonance with a molecular state. However, this regime induces too many relaxation errors due to resonant charge excitation. Therefore it is best to detune the flip-flop qubits from the molecular states, while still keeping a substantial inter-qubit coupling rate, via a second-order process, equal to:

$$g_{2q}^{\text{ff}} = g_{\text{so},1}g_{\text{so},2}\alpha\beta \left(\frac{1}{D_{\text{dd}} - \delta_{\text{so},1}} + \frac{1}{D_{\text{dd}} + \delta_{\text{so},2}} \right), \quad (16)$$

where D_{dd} is the charge eigenenergies shift and α, β the eigenstates coefficients – see Fig. 4c caption.

2-qubit gates start with both electrons at the interface, where qubits are decoupled since the electric dipoles and the hyperfine interactions are first-order insensitive to vertical electric fields. Indeed, from Eq. 16, g_{2q}^{ff} is negligible since g_{so} vanishes and δ_{so} diverges. The electrons are then simultaneously and adiabatically displaced to the ionization point for a time necessary for an \sqrt{i} SWAP gate, before returning to the interface. In Fig. 4d we show the dynamics of a 2-qubit gate performed with an adiabatic factor $K = 30$, following the trajectory shown in Fig. 4f. Similarly to 1-qubit z gates, the electron is first displaced in a fast time scale (~ 0.3 ns) set by the charge qubit parameters (ϵ_o and V_t), followed by a slower sweep (~ 19 ns) set by the spin-charge coupling parameters (δ_{so} and g_{so}), until it reaches the ionization point. The electron remains still for a short time before the whole process is then reversed. In the end a \sqrt{i} SWAP gate is performed. While some amount of charge is excited during the process, it goes back to its ground state, $|gg\rangle$, with an adiabatic error around 10^{-3} .

We quantify the 2-qubit gate fidelity in presence of the most deleterious noise types for our qubits, namely quasi-static E_z noise and charge-phonon relaxation. For this, we observe that the optimal gate fidelities are achieved when $E_z(\tau_{\sqrt{i}\text{SWAP}}/2) \approx E_z^0$. Similarly to 1-qubit x -gates, this happens because \sqrt{i} SWAP gates are sensitive to gate time jitter, and therefore errors are minimized at the CQSS where g_{2q}^{ff} is robust against E_z noise to first order – recall Fig. 4f and Eq. 16). An optimization algorithm finds the best adiabatic factor K that minimizes errors due to E_z noise for each value of $V_{t,1} = V_{t,2} = V_t$. The result is shown in Fig. 4g. Smaller detunings δ_{so} (small V_t) result in shorter gate times, which in turn reduces errors from quasi-static noise. However, this also implies more charge states in the qubit eigenstates, which slightly increases relaxation errors. The lowest

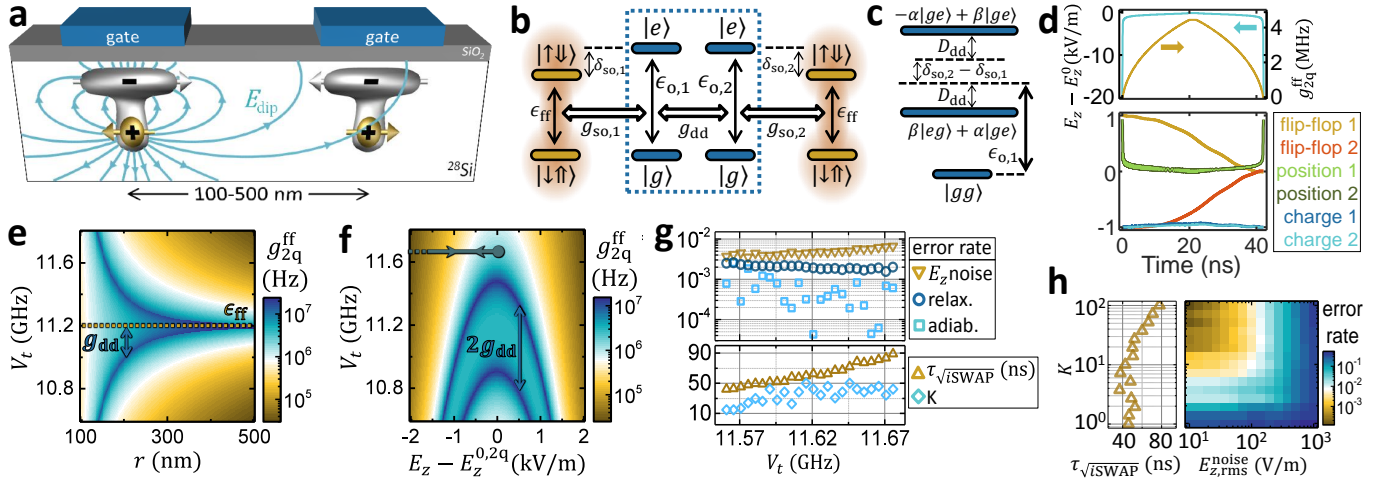


FIG. 4. **High-fidelity adiabatic \sqrt{i} SWAP gates between two distant flip-flop qubits via electric dipole-dipole interactions.** **a**, Device scheme for coupling qubits, showing dipole field lines, \mathbf{E}_{dip} , produced by the dipole on the left. **b**, Level diagram for two-qubit coupling via direct dipole-dipole interaction. **c**, Lowest molecular eigenstates for the two charge qubits inside dashed rectangle in **b**. Eigenenergy shift equals $D_{\text{dd}} = (\delta_{\text{so},2} - \delta_{\text{so},1}) (1 + [2g_{\text{dd}}/(\delta_{\text{so},2} - \delta_{\text{so},1})]^2) / 2$. Eigenstate coefficients are $\beta = \theta/\sqrt{\theta^2 + 1}$ and $\alpha = \phi/\sqrt{\phi^2 + 1}$, with $\theta, \phi = [(\delta_{\text{so},2} - \delta_{\text{so},1}) \pm \sqrt{(\delta_{\text{so},2} - \delta_{\text{so},1})^2 + (2g_{\text{dd}})^2}] / (2g_{\text{dd}})$. **d**, Time evolution of an adiabatic \sqrt{i} SWAP gate, for $K = 30$, $r = 180$ nm, $B_0 = 0.4$ T and $V_t = 11.58$ GHz. Effective coupling between 2 flip-flop qubits as a function of $V_{t,1} = V_{t,2} = V_t$, interdistance r (**e**) and electric field $E_{z,1} = E_{z,2} = E_z$ (**f**). Upper arrows in **f** represent adiabatic path followed for 2-qubit gates. $E_z^{0,2q} = E_z^0 - 2g_{\text{dd}}h/(2eL_i)$. **g**, Optimized \sqrt{i} SWAP gate errors, time and adiabatic factor K . **h**, Optimized error rate due to quasi-static E_z -noise for different noise amplitudes and adiabatic factor K (which sets the gate time).

error rates, $\sim 3 \times 10^{-3}$ are found at small detunings, $V_t - \epsilon_{\text{ff}} - g_{\text{dd}} \approx 100$ MHz ($V_t \approx 11.59$ GHz). At smaller detunings, the 2-qubit coupling rate is too fast, which requires faster adiabatic sweeps to avoid over-rotation (lower K , Fig. 4g), generating more leakage errors. The gate errors remain within $10^{-3} - 10^{-2}$ for a wide range of V_t . Finally, we estimate in Fig. 4h how noise errors depend on the noise amplitude and adiabatic factor K , which sets the gate time.

Our proposed 2-qubit gates are not only highly protected against noise, but also robust against donor misplacement. Indeed, variations in r , d_1 and d_2 mainly cause variations in g_{dd} , therefore simply changing the energy separation between molecular charge states (Fig. 4c). This does not modify g_{2q}^{ff} substantially, provided that V_t can be tuned accordingly (Fig. 4e) – following *e.g.* the method discussed in Supplementary Information S2. A limit is reached when $D_{\text{dd}} \ll \delta_{\text{so},i}$, resulting in negligible g_{2q}^{ff} because of the opposite signs in Eq. 16. Still, 2-qubit gates are highly effective for inter-qubit separations around 100 – 500 nm (or even larger since the metallic interface on top vertical dipoles increase their interaction – see Supplementary Information S4) or, equivalently, two orders of magnitude tolerance in g_{dd} . In particular, 2-qubit gate speeds do not decay with r^3 , as opposed to standard dipole-dipole coupling schemes^{26,31}. They are similarly fast and robust for 2nd- and 3rd-nearest neighbors, opening up new connectivity possibilities for a large-scale quantum processor⁵¹. The large tolerance in g_{dd} also accommodates very well the

donor depth uncertainties inherent to ion implantation⁵⁰, given the linear dependence of g_{2q}^{ff} on d_i (Eqs. 14b and 15).

We conclude that our scheme provides a dramatic reduction in the fabrication complexity, especially compared to schemes that require placing a gate *between* a pair of tightly-spaced donors, such as the Kane’s proposal¹⁵, which requires $r \approx 15$ nm separation between two ³¹P nuclear spins.

Scaling up using circuit quantum electrodynamics

In order to reach the long-term goal of a large-scale quantum processor, wiring up the control and read-out lines for each individual qubit is not trivial, given the high-density that spin qubits imply⁵². Recent solutions include cross-wiring using multilayer lithography²⁶ or floating gate electrodes inspired by dynamic random access memory systems⁵³. In both cases, using flip-flop qubits with long-distance interactions would result in widely spaced donors and loose fabrication tolerances. In addition, since flip-flop qubits are coupled via electric fields, they could be spaced further apart by using electrical mediators. These include floating metal gates⁵⁴ or even microwave resonators. Indeed, the use of electric dipole transitions allows a natural integration of donor-based spin qubits into a circuit-Quantum Electrodynamics (QED) architecture^{44,55–57} (see Fig. 5c for a possible device layout).

A full quantum mechanical treatment yields a charge-

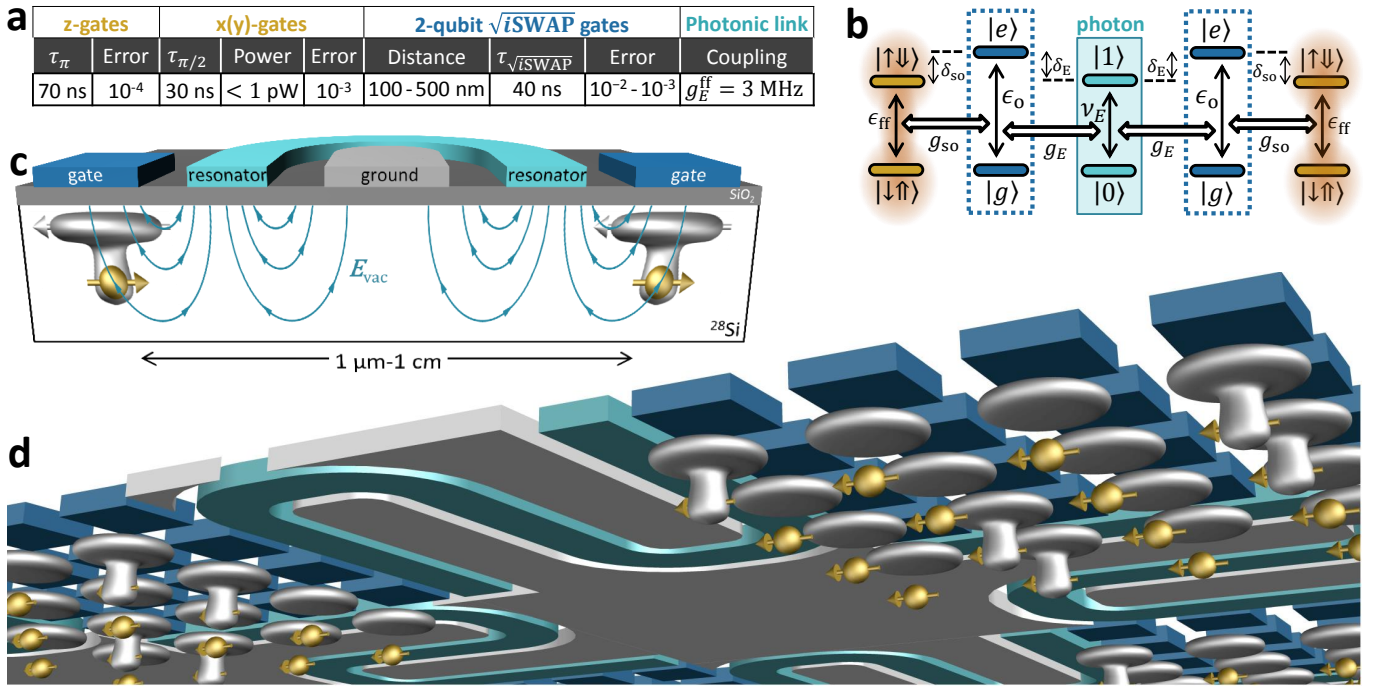


FIG. 5. **Silicon hybrid quantum processor.** **a**, Figures of merit summarizing the speed and error rates of different gate schemes presented in this paper, assuming realistic noise sources. **b**, Level diagram for distant flip-flop qubit coupling via a microwave resonator showing first photon levels and off-resonant charge states. **c**, Device scheme for coupling qubits via a photonic link. Distant donors, placed next to the resonator center line and biased to their ionization point, are subject to the vacuum electric field E_{vac} of a shared microwave resonator. **d**, Schematic view of a large-scale quantum processor based upon ^{31}P donors in Si, operated and coupled through the use of an induced electric dipole. Idle qubits have electron at interface, leaving the ^{31}P nucleus in the ultra-coherent ionized state. Electrons are partially shifted towards the donor for quantum operations. Sketch shows a possible architecture where a cluster of qubits is locally coupled via the electric dipole, and a subgroup thereof is further coupled to another cluster through interaction with a shared microwave cavity (aqua). The drawing is not to scale; control lines and readout devices are not shown.

photon coupling rate given by Eq. 13, with ν_E now representing the resonator fundamental mode frequency and E_{ac} the resonator vacuum field, E_{vac} . Again, it is best to have the charge excited state detuned from the flip-flop transition and resonator photon (see Fig. 5b), therefore minimizing charge excitation while retaining a second-order flip-flop-photon coupling given by Eq. 12. Assuming $\delta_{\text{so}} \approx \delta_E \approx 10g_{\text{so}} \approx 10g_E$, a $d = 15$ nm deep ^{31}P flip-flop qubit would be coupled to photons at a $g_E^{\text{ff}} \approx 3$ MHz rate. This is three orders of magnitude faster than the electron-spin coupling rate to a resonator via its magnetic vacuum field^{58,59}, and comparable to the coupling strength obtained by using strong magnetic field gradients^{60,61}, but without the need to integrate magnetic materials within a superconducting circuit. This assumes a vacuum field amplitude $E_{\text{vac}} \approx 30$ V/m, which can be obtained by using tapered coplanar waveguide or high-inductance resonators⁶².

The possibility of coupling the qubits to microwave photons provides a path for dispersive qubit readout, as well as for photonic interconnects. Near-quantum limited amplifiers have recently become available to obtain excellent readout speed and fidelities⁶³. The resonator can also be used as a quantum bus to couple two spin

qubits separated by as far as 1 cm (Fig. 5c), a distance given by the mode wavelength. Fig. 5b shows the detailed energy level diagram. To avoid losses from photon decay, the qubits should be detuned from the resonator by an amount much greater than the qubit-photon coupling rates. Assuming $\delta_E^{\text{ff}} = 10g_E^{\text{ff}}$, where $\delta_E^{\text{ff}} = \nu_E - \epsilon_{\text{ff}}$, the effective 2-qubit coupling $g_{2q}^{\text{ff}} \approx (g_E^{\text{ff}})^2 / \delta_E^{\text{ff}} \approx 0.3$ MHz yields a \sqrt{i} SWAP gate that takes only $0.4 \mu\text{s}$.

Outlook: building a quantum processor

Fig. 5a summarizes the key figures of merit of a quantum processor based on flip-flop qubits coupled by electric dipole interactions. Fast 1-qubit x -gates are attainable with low electric drive power and error rates $\sim 10^{-3}$. 2-qubit \sqrt{i} SWAP gates are fast and with error rates approaching 10^{-3} . At the end of all operations, the phase of each qubit can be corrected, via adiabatic z -gates, in fast time scales and low error rates $\sim 10^{-4}$. These values are based on current experimentally known values of charge noise in silicon devices⁴⁰, and are possibly amenable to improvement through better control of the fabrication parameters. More advanced control pulse schemes could allow for faster gates with less leakage^{67? -69}, and active

noise cancellation techniques, *e.g.* pulses for gate time jitter⁷⁰ or decoherence⁷¹ suppression, could further improve gate fidelities.

Idle qubits are best decoupled from all other qubits by having the electron at the interface and the quantum state stored in the nuclear spin, which has a record coherence times $T_2 \gtrsim 30$ s (ref. 7), and can be even longer in bulk samples⁶. Quantum information can be swapped between the nuclear and the flip-flop qubit by simply applying an ESR π -pulse that excites the $|\downarrow\downarrow\rangle$ state to $|\uparrow\downarrow\rangle$ (Fig. 1).

Qubit read-out can be obtained by spin-dependent tunneling into a cold charge reservoir, detected by a single-electron transistor¹⁸. Read-out times can be ~ 1 μ s with cryogenic amplifiers⁶⁴, which is comparable to the time necessary to perform, for example, ~ 20 individual gates lasting ~ 50 ns each, in a surface code error correction protocol².

A large-scale, fault-tolerant architecture can be built in a variety of ways. One- or two-dimensional arrays can be built to implement error correction schemes such as the Steane⁶⁵ or the surface² code, since all mutual qubit couplings are tunable and gateable. A larger processor can include a hybrid of both coupling methods, incorporating cells of dipolarly-coupled qubits, interconnected by microwave photonic links (Fig. 5), in which case more advanced error-correction codes can be implemented^{1,3,4,51}. Microwave resonators could be also used to interface donors with superconducting qubits^{8,66}, for the long-term goal of a hybrid quantum processor that benefits from the many advantages of each individual architecture⁵⁶.

In conclusion, we have presented a novel way to encode quantum information in the electron-nuclear spin states of ³¹P donors in silicon, and to realize fast, high-fidelity, electrically-driven universal quantum gates. Our proposal provides a credible pathway to the construction of a large-scale quantum processor where atomic-size spin qubits are integrated with silicon nanoelectronic devices, in a platform that does not require atomic-scale precision in the qubit placement. The qubits are naturally amenable to being placed on two-dimensional grids and, with realistic assumptions on noise and imperfections, are predicted to achieve error rates compatible with fault-tolerant quantum error correction.

METHODS

Adiabaticity

Given a time-dependent Hamiltonian in a 2-dimensional Hilbert space,

$$\mathcal{H}_2 = \Delta(t)\sigma_z + \Omega(t)\sigma_x, \quad (17)$$

in units of rad/s, the adiabatic condition is expressed as⁷²

$$K = \left| \frac{\omega_{\text{eff}}}{\dot{\alpha}} \right| \gg 1, \quad (18)$$

where $\omega_{\text{eff}} = \sqrt{\Delta^2 + \Omega^2}$ is the instantaneous transition angular frequency between eigenstates, and $\dot{\alpha}$ is the rate of change of the orientation of ω_{eff} ($\alpha = \arctan(\Omega/\Delta)$). It follows from Eq. 18 that

$$K = \frac{(\Delta^2 + \Omega^2)^{3/2}}{|\dot{\Delta}\Omega - \dot{\Omega}\Delta|} \gg 1, \quad (19)$$

Although the processes described in this paper involve multiple levels, we applied Eq. 19 in different forms as an approximation of adiabaticity. This was confirmed to be always valid by checking that the leakage errors were kept below a target level.

In particular, for 1-qubit z-gates and 2-qubit \sqrt{i} SWAP gates, we used $\Delta_c = \pi e(E_z - E_z^0)d/h$ and $\Omega_c = \pi V_t$ to find K_c for the charge qubit, and $\Delta_{\text{so}} = \pi \delta_{\text{so}}$ and $\Omega_{\text{so}} = 2\pi g_{\text{so}}$ to find K_{so} for the spin-charge coupling. For a chosen adiabatic factor K , we find $E_z(t)$ by satisfying the condition $\min(K_{\text{so}}, K_c) = K$.

For 1-qubit drive, we used $\Delta_E = \pi \delta_E$ and $\Omega_E = 2\pi g_E$ to find K_E . A particular choice of $K = K_E$ sets the adiabatic sweep rate of $E_{\text{ac}}(t)$.

Estimation of dephasing and gate errors

In order to estimate the effects of quasi-static E_z noise on dephasing, we first calculate the flip-flop qubit transition frequency ϵ_{ff} (difference between eigenfrequencies corresponding to eigenstates closest to $|g \downarrow\uparrow\rangle$ and $|g \uparrow\downarrow\rangle$, which we denote as $|g \downarrow\uparrow\rangle_e$ and $|g \uparrow\downarrow\rangle_e$). Next, for an equally distributed noise range $E_z^n = \sqrt{3}[-E_{z,\text{rms}}^{\text{noise}}, E_{z,\text{rms}}^{\text{noise}}]$, we estimate the qubit dephasing rate to be

$$\text{Dephasing rate} = \sum_n |\epsilon_{\text{ff}} - \epsilon_{\text{ff}}^n| / N_n, \quad (20)$$

where N_n is the number of sampled E_z^n and ϵ_{ff}^n is calculated for each value of E_z^n .

The averaged error rate (without noise) of a desired adiabatic unitary process U_{ideal} is calculated by averaging the fidelity of the actual process U over a set of initial states $|j\rangle$,

$$\text{Adiabatic error} = 1 - \sum_{|j\rangle} |\langle j| U^\dagger U_{\text{ideal}} |j\rangle|^2 / N_j, \quad (21)$$

where N_j is the number of initial states. For 1-qubit gates (*e.g.* a π z-gate or a $\pi/2$ x(y)-gate), we choose $|j\rangle = \{|g \downarrow\uparrow\rangle_e, |g \uparrow\downarrow\rangle_e, (|g \downarrow\uparrow\rangle_e + |g \uparrow\downarrow\rangle_e)/\sqrt{2}, (|g \downarrow\uparrow\rangle_e - |g \uparrow\downarrow\rangle_e)/\sqrt{2}\}$ and $N_j = 4$, whereas for 2-qubit gates (*e.g.* \sqrt{i} SWAP) $|j\rangle = |j\rangle_1 \otimes |j\rangle_2$ (the 1, 2 indexes refer to the aforementioned 4 initial states for each qubit) and $N_j = 16$.

To estimate the averaged gate error rate under quasi-static E_z noise, the actual process U and eigenstates $|j\rangle$ are calculated for each value of E_z^n before averaging,

$$\text{Noise error} = 1 - \sum_{n, |j\rangle_n} |\langle j|_n U_n^\dagger U_{n, \text{ideal}} |j\rangle_n|^2 / (N_j N_n) \quad (22)$$

Finally, to estimate errors due to charge-phonon relaxation, we multiply the averaged charge excitation by its relaxation rate and assume an exponential decay in fi-

delity:

$$\text{Relax. error} = \frac{1 - e^{-\int_0^{\tau_{\text{gate}}} \left(\sum_{|j(t)\rangle} \langle j(t)|e\rangle \langle e|j(t)\rangle / N_j \right) dt / T_{1,o}}}{2}, \quad (23)$$

where $|j(t)\rangle$ are the time-evolution of the initial set states $|j\rangle$. For 2-qubit gates, we sum up the error rate of each qubit.

-
- ¹ Terhal, B. M. Quantum error correction for quantum memories. *Rev. Mod. Phys.* **87**, 307 (2015).
- ² Fowler, A. G., Mariantoni, M., Martinis, J. M. & Cleland, A. N. Surface codes: Towards practical large-scale quantum computation. *Phys. Rev. A* **86**, 032324 (2012).
- ³ Knill, E. Quantum computing with realistically noisy devices. *Nature* **434**, 39–44 (2005).
- ⁴ Nickerson, N. H., Li, Y. & Benjamin, S. C. Topological quantum computing with a very noisy network and local error rates approaching one percent. *Nature Commun.* **4**, 1756 (2013).
- ⁵ Maurer, P. C. *et al.* Room-temperature quantum bit memory exceeding one second. *Science* **336**, 1283–1286 (2012).
- ⁶ Saeedi, K., Simmons, S., Salvail, J. Z., Dluhy, P., Riemann, H., Abrosimov, N. V., Becker, P., Pohl, H.-J., Morton, J. J. L. & Thewalt, M. L. W. Room-temperature quantum bit storage exceeding 39 minutes using ionized donors in silicon-28. *Science* **342**, 830–833 (2013).
- ⁷ Muhonen, J. T. *et al.* Storing quantum information for 30 seconds in a nanoelectronic device. *Nature Nanotech.* **9**, 986–991 (2014).
- ⁸ Barends, R. *et al.* Superconducting quantum circuits at the surface code threshold for fault tolerance. *Nature* **508**, 500–503 (2014).
- ⁹ Harty, T. P., Allcock, D. T. C., Ballance, C. J., Guidoni, L., Janacek, H. A., Linke, N. M., Stacey, D. N. & Lucas, D. M. High-fidelity preparation, gates, memory, and readout of a trapped-ion quantum bit. *Phys. Rev. Lett.* **113**, 220501 (2014).
- ¹⁰ Veldhorst, M. *et al.* An addressable quantum dot qubit with fault-tolerant control-fidelity. *Nature Nanotech.* **9**, 981–985 (2014).
- ¹¹ Muhonen, J. T. *et al.* Quantifying the quantum gate fidelity of single-atom spin qubits in silicon by randomized benchmarking. *Journal of Physics: Condensed Matter* **27**, 154205 (2015).
- ¹² Benhelm, J., Kirchmair, G., Roos, C. F. & Blatt, R. Towards fault-tolerant quantum computing with trapped ions. *Nature Physics* **4**, 463–466 (2008).
- ¹³ Zwanenburg, F. A., Dzurak, A. S., Morello, A., Simmons, M. Y., Hollenberg, L. C., Klimeck, G., Rogge, S., Copper-Smith, S. N. & Eriksson, M. A. Silicon quantum electronics. *Rev. Mod. Phys.* **85**, 961 (2013).
- ¹⁴ Itoh, K. M. & Watanabe, H. Isotope engineering of silicon and diamond for quantum computing and sensing applications. *MRS Communications* **4**, 143–157 (2014).
- ¹⁵ Kane, B. E. A silicon-based nuclear spin quantum computer. *Nature* **393**, 133–137 (1998).
- ¹⁶ Koiller, B., Hu, X. & Das Sarma, S. Exchange in silicon-based quantum computer architecture. *Phys. Rev. Lett.* **88**, 027903 (2002).
- ¹⁷ Song, Y. & Das Sarma, S. Statistical exchange-coupling errors and the practicality of scalable silicon donor qubits. *Appl. Phys. Lett.* **109**, 253113 (2016).
- ¹⁸ Morello, A. *et al.* Single-shot readout of an electron spin in silicon. *Nature* **467**, 687–691 (2010).
- ¹⁹ Pla, J. J., Tan, K. Y., Dehollain, J. P., Lim, W. H., Morton, J. J. L., Jamieson, D. N., Dzurak, A. S. & Morello, A. A single-atom electron spin qubit in silicon. *Nature* **489**, 541–545 (2012).
- ²⁰ Pla, J. J., Tan, K. Y., Dehollain, J. P., Lim, W. H., Morton, J. J. L., Zwanenburg, F. A., Jamieson, D. N., Dzurak, A. S. & Morello, A. High-fidelity readout and control of a nuclear spin qubit in silicon. *Nature* **496**, 334–338 (2013).
- ²¹ Laucht, A. *et al.* Electrically controlling single-spin qubits in a continuous microwave field. *Science Adv.* **1**, e1500022 (2015).
- ²² Dehollain, J. P., Muhonen, J. T., Tan, K. Y., Saraiva, A., Jamieson, D. N., Dzurak, A. S. & Morello, A. Single-shot readout and relaxation of singlet and triplet states in exchange-coupled ³¹P electron spins in silicon. *Phys. Rev. Lett.* **112**, 236801 (2014).
- ²³ Gonzalez-Zalba, M. F., Saraiva, A., Calderón, M. J., Heiss, D., Koiller, B. & Ferguson, A. J. An exchange-coupled donor molecule in silicon. *Nano letters* **14**, 5672–5676 (2014).
- ²⁴ Weber, B., Matthias, T. H., Mahapatra, S., Watson, T. F., Ryu, H., Rahman, R., L., H. C., Klimeck, G. & Simmons, M. Y. Spin blockade and exchange in coulomb-confined silicon double quantum dots. *Nature Nanotech.* **9**, 430–435 (2014).
- ²⁵ Kalra, R., Laucht, A., Hill, C. D. & Morello, A. Robust two-qubit gates for donors in silicon controlled by hyperfine interactions. *Phys. Rev. X* **4**, 021044 (2014).
- ²⁶ Hill, C. D., Peretz, E., Hile, S. J., House, M. G., Fuechsle, M., Rogge, S., Simmons, M. Y. & Hollenberg, L. C. L. A surface code quantum computer in silicon. *Science Advances* **1**, e1500707 (2015).
- ²⁷ Hollenberg, L. C. L., Greentree, A. D., Fowler, A. G. & Wellard, C. J. Two-dimensional architectures for donor-based quantum computing. *Phys. Rev. B* **74**, 045311 (2006).
- ²⁸ Mohiyaddin, F. *et al.* Transport of spin qubits with donor chains under realistic experimental conditions. *Phys. Rev. B* **94**, 045314 (2016).
- ²⁹ Morton, J. L. A silicon-based cluster state quantum computer. *arXiv:0905.4008* (2009).
- ³⁰ Trifunovic, L., Pedrocchi, F. L. & Loss, D. Long-distance

- entanglement of spin qubits via ferromagnet. *Phys. Rev. X* **3**, 041023 (2013).
- ³¹ O’Gorman, J., Nickerson, N. H., Ross, P., Morton, J. J. & Benjamin, S. C. A silicon-based surface code quantum computer. *npj Quantum Information* **2**, 15019 (2016).
- ³² Pica, G., Lovett, B. W., Bhatt, R. N., Schenkel, T. & Lyon, S. A. Surface code architecture for donors and dots in silicon with imprecise and nonuniform qubit couplings. *Phys. Rev. B* **93**, 035306 (2016).
- ³³ Calderón, M. J., Koiller, B., Hu, X. & Das Sarma, S. Quantum control of donor electrons at the Si-SiO₂ interface. *Phys. Rev. Lett.* **96**, 096802 (2006).
- ³⁴ Lansbergen, G. P. *et al.* Gate-induced quantum-confinement transition of a single dopant atom in a silicon finfet. *Nature Phys.* **4**, 656–661 (2008).
- ³⁵ Laird, E. A., Barthel, C., Rashba, E. I., Marcus, C. M., Hanson, M. P. & Gossard, A. C. Hyperfine-mediated gate-driven electron spin resonance. *Phys. Rev. Lett.* **99**, 246601 (2007).
- ³⁶ Luo, Y., Yu, H. & Yao, W. Deterministic preparation of Dicke states of donor nuclear spins in silicon by cooperative pumping. *Phys. Rev. B* **85**, 155304 (2012).
- ³⁷ Klimeck, G. *et al.* Atomistic simulation of realistically sized nanodevices using NEMO 3-D – part i: Models and benchmarks. *IEEE Transactions on Electron Devices* **54**, 2079–2089 (2007).
- ³⁸ Kim, D. *et al.* Microwave-driven coherent operation of a semiconductor quantum dot charge qubit. *Nature Nanotech.* **10**, 243–247 (2015).
- ³⁹ Rahman, R., Park, S. H., Boykin, T. B., Klimeck, G., Rogge, S. & Hollenberg, L. C. L. Gate-induced *g*-factor control and dimensional transition for donors in multivalley semiconductors. *Phys. Rev. B* **80**, 155301 (2009).
- ⁴⁰ Freeman, B. M., Schoenfeld, J. S., Jiang, H. Comparison of low frequency charge noise in identically patterned Si/SiO₂ and Si/SiGe quantum dots. *Appl. Phys. Lett.* **108**, 253108 (2016).
- ⁴¹ Thorgrimsson, B. *et al.* Mitigating the effects of charge noise and improving the coherence of a quantum dot hybrid qubit. *arXiv:1611.04945* (2016).
- ⁴² Harvey-Collard, P. *et al.* Nuclear-driven electron spin rotations in a single donor coupled to a silicon quantum dot. *arXiv:1512.01606* (2015).
- ⁴³ Boross, P., Széchenyi, G., Pályi, A. Valley-enhanced fast relaxation of gate-controlled donor qubits in silicon. *Nanotechnology* **27**, 314002 (2016).
- ⁴⁴ Blais, A., Huang, R.-S., Wallraff, A., Girvin, S. M. & Schoelkopf, R. J. Cavity quantum electrodynamics for superconducting electrical circuits: An architecture for quantum computation. *Phys. Rev. A* **69**, 062320 (2004).
- ⁴⁵ Calderón, M. J., Koiller, B. & Das Sarma, S. Model of valley interference effects on a donor electron close to a Si/SiO₂ interface. *Phys. Rev. B* **77**, 155302 (2008).
- ⁴⁶ Wolfowicz, G. *et al.* Atomic clock transitions in silicon-based spin qubits. *Nature Nanotech.* **8**, 561–564 (2013).
- ⁴⁷ Oh, S., Shim, Y., Fei, J., Friesen, M. & Hu, X. Resonant adiabatic passage with three qubits. *Phys. Rev. B* **87**, 022332 (2013).
- ⁴⁸ Henkel, C., Pötting, S. & Wilkens, M. Loss and heating of particles in small and noisy traps. *App. Phys. B* **69**, 379–387 (1999).
- ⁴⁹ Ravets, S., Labuhn, H., Barredo, D., Beguin, L., Lahaye, T. & Browaeys, A. Coherent dipole-dipole coupling between two single rydberg atoms at an electrically-tuned forster resonance. *Nature Phys.* **10**, 914–917 (2014).
- ⁵⁰ van Donkelaar, J. *et al.* Single atom devices by ion implantation. *J. Phys.: Condens. Matter* **27**, 154204 (2015).
- ⁵¹ Li, Y. *et al.* Interfacing spin qubits in quantum dots and donors - hot, dense and coherent. *arXiv:1612.05936* (2016).
- ⁵² Vandersypen, L. M. K. & Benjamin, S. C. One-dimensional quantum computing with a ‘segmented chain’ is feasible with today’s gate fidelities. *arXiv:1702.05657* (2017).
- ⁵³ Veldhorst, M., Eenink, H. G. J., Yang, C. H. & Dzurak, A. S. Silicon CMOS architecture for a spin-based quantum computer. *arXiv:1609.09700* (2016).
- ⁵⁴ Trifunovic, L. *et al.* Long-distance spin-spin coupling via floating gates. *Phys. Rev. X* **2**, 011006 (2012).
- ⁵⁵ Childress, L., Sørensen, A. S. & Lukin, M. D. Mesoscopic cavity quantum electrodynamics with quantum dots. *Phys. Rev. A* **69**, 042302 (2004).
- ⁵⁶ Xiang, Z.-L., Ashhab, S., You, J. Q. & Nori, F. Hybrid quantum circuits: Superconducting circuits interacting with other quantum systems. *Rev. Mod. Phys.* **85**, 623–653 (2013).
- ⁵⁷ X. Mi *et al.* Strong coupling of a single electron in silicon to a microwave photon. *Science* (2016).
- ⁵⁸ Tosi, G., Mohiyaddin, F. A., Huebl, H. & Morello, A. Circuit-quantum electrodynamics with direct magnetic coupling to single-atom spin qubits in isotopically enriched ²⁸Si. *AIP Advances* **4**, 087122 (2014).
- ⁵⁹ Haikka, P. *et al.* Proposal for detecting a single electron spin in a microwave resonator. *Phys. Rev. A* **95**, 022306 (2017).
- ⁶⁰ Hu, X., Liu, Y.-x. & Nori, F. Strong coupling of a spin qubit to a superconducting stripline cavity. *Phys. Rev. B* **86**, 035314 (2012).
- ⁶¹ Viennot, J. J., Dartiailh, M. C., Cottet, A. & Kontos, T. Coherent coupling of a single spin to microwave cavity photons. *Science* **349**, 408–411 (2015).
- ⁶² Samkharadze, N. *et al.* High-kinetic-inductance superconducting nanowire resonators for circuit QED in a magnetic field. *Phys. Rev. X* **5**, 044004 (2016).
- ⁶³ Castellanos-Beltran, M., Irwin, K., Hilton, G., Vale, L. & Lehnert, K. Amplification and squeezing of quantum noise with a tunable Josephson metamaterial. *Nature Phys.* **4**, 929–931 (2008).
- ⁶⁴ Curry, M. J. *et al.* Cryogenic preamplification of a single-electron-transistor using a silicon-germanium heterojunction-bipolar-transistor. *Appl. Phys. Lett.* **106**, 203505 (2015).
- ⁶⁵ Steane, A. Multiple-particle interference and quantum error correction. *Proceedings of the Royal Society of London A: Mathematical, Physical and Engineering Sciences* **452**, 2551–2577 (1996).
- ⁶⁶ Devoret, M. H. & Schoelkopf, R. J. Superconducting circuits for quantum information: an outlook. *Science* **339**, 1169–1174 (2013).
- ⁶⁷ Motzoi, F., Gambetta, J. M., Rebentrost, P. & Wilhelm, F. K. Simple Pulses for Elimination of Leakage in Weakly Nonlinear Qubits. *Phys. Rev. Lett.* **103**, 110501 (2009).
- ⁶⁸ Ghosh, J., Coppersmith, S. N. & Friesen, M. Pulse Sequences for Suppressing Leakage in Single-Qubit Gate Operations. *arXiv:1612.00568* (2016).
- ⁶⁹ Werschnik, J. & Gross, E. K. U. Quantum optimal control theory. *J. Phys. B: At. Mol. Opt. Phys.* **40**, R175 (2007).
- ⁷⁰ Hill, c. Robust controlled-NOT gates from almost any

- interaction. *Phys. Rev. Lett.* **98**, 180501 (2007)
- ⁷¹ van der Sar, T. *et al.* Decoherence-protected quantum gates for a hybrid solid-state spin register. *Nature* **484**, 82–86 (2012).
- ⁷² Garwood, M. & DelaBarre, L. The Return of the Frequency Sweep: Designing Adiabatic Pulses for Contemporary NMR. *J. Magn. Reson.* **153**, 155–177 (2001).

Acknowledgments We thank A. Blais, H. Bluhm, M. Eriksson, J. O’Gorman, S. Benjamin, J. Salfi, M. Veldhorst, A. Laucht, R. Kalra and C. A. Parra-Murillo for discussions. This research was funded by the Australian Research Council Centre of Excellence for Quantum Computation and Communication Technology (project number CE110001027), the US Army Research Office (W911NF-13-1-0024) and the Commonwealth Bank of Australia. Tight-biding simulations used NCN/nanohub.org computational resources funded by the US National Science Foundation under contract number EEC-1227110.

Author Contributions A.M. and G.T. conceived the project. G.T. developed the theoretical framework, with F.A.M.’s assistance and under A.M.’s supervision. G.T. and F.A.M. performed calculations and numerical simulations with S.T.’s and V.S.’s assistance. R.R. and G.K. developed the qubit simulation capabilities in the NEMO-3D code. G.T., A.M. and F.A.M. wrote the manuscript, with input from all co-authors.

Additional Information Supplementary information accompanies the paper. Correspondence and requests for materials should be addressed to G.T. (g.tosi@unsw.edu.au) or A.M. (a.morello@unsw.edu.au).

SUPPLEMENTARY INFORMATION for
“Silicon quantum processor with robust long-distance qubit couplings”, by G. Tosi *et al.*

S1. Validity of the two-level approximation for the electron orbital wavefunction

The concepts and calculations shown in the manuscript are based upon approximating the electron orbital degree of freedom as a two-level system, i.e. a charge qubit. The true orbital levels of a donor-interface system are, of course, more complex than that. However, below we show that the charge qubit model represents an excellent approximation, for the range of parameters relevant to our proposal.

The ground orbital wavefunction $|d\rangle$ of an electron bound to a donor is a symmetric combination of the 6 conduction band minima (“valleys”) ($k_{\pm x}$, $k_{\pm y}$, $k_{\pm z}$) in silicon^{S1}. Higher excited valley-orbit states are separated by > 10 meV and can be safely neglected. Conversely, the orbital states of an electron confined at the Si/SiO₂ interface comprise a low-energy doublet of states, with wavefunctions constructed as a combination of the $k_{\pm z}$ valleys. The k_{+z} and k_{-z} valleys are coupled by the abrupt potential of the interface, which breaks the degeneracy of the ground state doublet into the lower valley $|i\rangle$ and upper valley $|v\rangle$ states, separated by the valley splitting V_s ^{S2}. All the remaining excited donor and interface orbital states are well above the ground doublet by several meV^{S3,S4}. When the donor is close to ionization, the lowest-energy states of the system therefore consist of $|d\rangle$, $|i\rangle$ and $|v\rangle$ states, as shown in Fig. S1 inset.

We computed the above three energy levels with the atomistic tight binding package NEMO-3D^{S5,S6}, assuming a donor placed at depth $z_d = 15.2$ nm below the Si/SiO₂ interface, and biased close to the donor ionization field E_z^0 . The dependence of the energies of $|d\rangle$, $|i\rangle$ and $|v\rangle$ on electric field E_z is shown by the dots in Fig. S1. We also fit the lowest energy levels with the charge qubit two-level model described by the Hamiltonian \mathcal{H}_{orb} (in Eq. 2 of the main manuscript), and plot them as solid blue lines in Fig. S1. The two-level model agrees well with tight-binding calculation taking $V_t = 9.3$ GHz and $d = 11$ nm in Eq. 2. Here, d represents the separation between the center-of-mass positions of the donor-bound ($|d\rangle$) and interface-bound ($|i\rangle$) orbitals. This is the relevant quantity in calculating the electric dipole strength. The extracted value d is lower than the donor depth z_d , as expected, and is consistent with the separation between the mean positions of the donor and interface electron wavefunctions as modeled with NEMO-3D.

Fig. S1 shows that, when $E_z \ll E_z^0$, the orbital ground state $|g\rangle$ of the electron is localized at the donor, whereas the first excited state corresponds to the lower valley interface state. The two states are separated in energy by ϵ_o , given by Eq. 3 of the main manuscript. As E_z increases, the two states approach, and anticross at $E_z = E_z^0$. For $E_z \gg E_z^0$, the donor state will even-

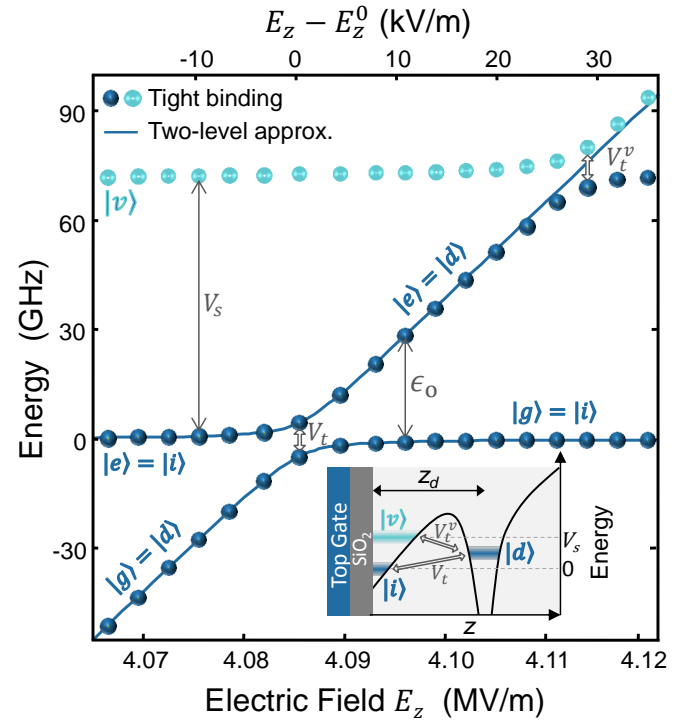


FIG. S1. Orbital and valley states. The lowest orbital energy levels of the donor-interface system, with respect to the lower valley interface state $|i\rangle$ (set as the zero-energy reference). The donor is assumed 15.2 nm below a Si/SiO₂ interface. The dots correspond to the energy levels obtained from a full-scale tight-binding calculation with NEMO-3D. Solid lines represent the energy levels obtained from the two level approximation described by Eq. 2 in the main manuscript. An excellent agreement between our two-level model and tight binding calculations is observed, since the valley splitting V_s is much larger than the tunnel coupling V_t . Inset: Potential profile as a function of depth, illustrating the donor $|d\rangle$, lower $|i\rangle$ and upper $|v\rangle$ valley interface states. The donor ground state is tunnel-coupled to the lower and upper valley interface states by V_t and V_t^v respectively.

tually (at $E_z \sim 4.11$ MV/m) anticross with the upper valley interface state. Therefore, as shown by the solid lines in Fig. S1, a two-level model described by the $|d\rangle$ and $|i\rangle$ states constitutes an excellent approximation for $E_z < E_z^0$. This allows a broad range of validity of the simple charge qubit model, provided the interface valley splitting V_s is much larger than the tunnel coupling V_t . The NEMO-3D model used here predicts $V_s = 71.7$ GHz, which is indeed much larger than $V_t = 9.3$ GHz. Experimentally, even higher values of V_s are routinely observed in electrons confined at the Si/SiO₂ interface by top-gated structures^{S7}, providing further reassurance on the practical validity of our models.

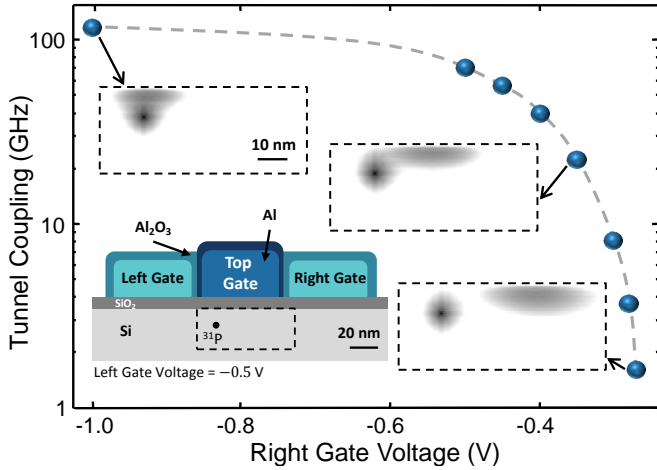


FIG. S2. **Gate-tunability of the tunnel coupling.** Tunnel coupling V_t of the charge qubit as a function of gate voltage. To tune V_t , additional gates (left and right) are present on either side of the top gate which pulls the ^{31}P donor electron to the interface. The insets illustrate the NEMO-3D wavefunctions, when $V_r = -1, -0.35$ and -0.27 V. $V_l = -0.5$ V for all the simulations, and the top gate is biased such that the position of the electron is in between the donor and interface. The donor is assumed to be $z_d = 9.2$ nm below a SiO_2 interface.

S2. Tunnel coupling tunability between donor and interface

The tunnel coupling V_t of the electron between the donor and interface orbital states plays a key role in our models. It influences all the driving strengths (Eqs. 8, 12 and 13) and inter-qubit couplings (Eq. 16). In the presence of a single metal gate above the donor location, the dependence of V_t on donor depth has been analyzed with effective mass theory^{S4,S8}. Ref. S8 indicates that V_t depends exponentially on donor depth z_d , and decreases by an order of magnitude for every 6 nm increase in z_d . Moreover, in addition to the exponential decay, the tunnel coupling also has an oscillatory dependence on z_d at the atomic scale due to valley interference effects^{S8}.

Using the ion implantation technique, the placement of a donor at $z_d \approx 15$ nm below the interface with a 5 nm thick oxide results in a vertical uncertainty of order ± 10 nm (ref. S9), resulting in more than 2 orders of magnitude uncertainty in V_t . Therefore, it is crucial to implement a method to tune V_t *in situ*.

Here, we propose that V_t can be controlled by adding two gates (left and right) on either side of the gate (top) which pulls the donor electron to the interface. The relative voltages V_l and V_r applied to the left and right gates respectively can modify the potential landscape, and displace laterally the location of the interface wavefunction. This, in turn modifies the distance between the donor and interface wavefunctions allowing V_t to be significantly reduced. We use a combination of a finite element Poisson solver^{S10} and NEMO-3D to estimate V_t in this device topology. In Fig. S2 we plot the tunnel coupling tun-

ability as a function of V_r , assuming $V_l = -0.5$ V and $z_d = 9.2$ nm. The insets of Fig. S2 show the NEMO-3D electron wavefunctions, when the top gate is biased such that the mean position of the electron is in between the donor and interface. We infer that the electron wavefunction at the interface can be moved by several tens of nanometers with V_r , allowing V_t to be tuned by at least ~ 2 orders of magnitude. This technique therefore enables us to circumvent the uncertainty in donor depth and V_t arising from ion-implantation, while remaining straightforward from a nanofabrication point of view. Note that, by relocating the problem of valley oscillations from the exchange interaction (Kane proposal) to the tunnel coupling (our proposal), we have effectively provided a way in which the delicate parameter can now be tuned using a much simpler gate geometry. Indeed, the gate layout used in this model is essentially identical to the layout routinely adopted for the fabrication of electrostatically-defined quantum dots at the Si/SiO_2 interface^{S7,S11}. These results indicate that a viable strategy for the construction of an ion-implanted quantum processor based upon our idea is to aim for an implantation depth that is by default rather shallow, then reduce V_t locally with the use of the surface gate stack.

S3. Charge and gate noise

In the main manuscript, we have presented estimates of dephasing rates and gate errors extracted from models where we assume a quasi-static (i.e. with a spectral weight centered at frequencies smaller than the qubit resonance and the Rabi frequency) electric field noise acting on the qubits. Here we explain why this assumption, and the r.m.s. value of 100 V/m for the noise, is justified for silicon nanoelectronic devices.

Given that the distance between the donor and interface sites is ~ 10 -30 nm, a vertical noise field of 100 V/m would correspond to 1-3 μeV charge detuning noise. This is consistent with the 1-9 μeV noise found in a range of semiconductor nanodevices, including SiGe ^{S12-S14}, AlGaAs ^{S15} and Si/SiO_2 ^{S14,S16}. In particular, MOS structures were found recently to have similar charge noise levels as SiGe devices, around 1.5 μeV .

The particular geometry of our qubits contributes to making them less susceptible to device-intrinsic charge noise. First of all, the electric dipole induced on a donor 15 nm below the Si/SiO_2 interface is substantially smaller than that of lateral gate-defined double quantum dots. Second, our qubits are largely insensitive to horizontal charge noise. Indeed, the orientation of the donor-interface dipole is mostly vertical (even when the interface wavefunction is displaced laterally, since image charges screen the lateral dipole – see Supplementary Information S4). The only effect of lateral noise is to modulate V_t – see Supplementary Information S2. For $V_t \approx 10$ GHz, Fig. S2 suggests that 10 μV r.m.s. lateral noise would cause less than 1% uncertainty in δ_{so} (and

therefore in gate time), which translates into maximum 10^{-4} errors due to gate time jitter for the flip-flop qubit, well below other contributions, and maximum $\sim 10^4$ Hz extra dephasing due to dispersive shifts (Eq. 9).

Another source of vertical electric field noise can be the thermal and electrical noise produced by the metallic gates on top of the qubits, and the room-temperature instruments they connect to. An $R = 50 \Omega$ resistor at room temperature produces Johnson-Nyquist noise with an r.m.s voltage $\sqrt{4k_B T R \Delta\nu}$. Therefore a quasi-static bandwidth $\Delta\nu \sim 10^6$ Hz produces $\sim 1 \mu\text{V}$ voltage noise, which is equivalent to $E_{z,\text{rms}}^{\text{noise}} \sim 10 \text{ V/m}$, or errors $< 10^{-5}$ (Fig. 3g). Furthermore, because of the very low powers required by the electrically-driven 1-qubit gates and adiabatic shuttling, it is possible to insert abundant low-temperature attenuation along the high-frequency lines, and therefore the relevant temperature for the Johnson-Nyquist noise is well below room temperature. On the other hand, being close to a metallic interface, our qubit will be subject to evanescent wave Johnson noise (EWJN) due to vacuum fluctuations. Assuming the qubit is $z = 15 \text{ nm}$ under aluminum gates at $T = 100 \text{ mK}$ ($\sigma = 1.4 \times 10^8 \text{ S/m}$ conductivity^{S17}), a quasi-static bandwidth $\Delta\nu \approx 10^6$ Hz produces^{S18} $\sqrt{k_B T \Delta\nu / (2z^3 \sigma)} \sim 0.04 \text{ V/m}$ r.m.s. electric field noise, therefore negligible. We conclude that the main source of quasi-static noise will be charge noise with a typical $1/\nu$ spectrum. To get $E_{z,\text{rms}}^{\text{noise}} = 100 \text{ V/m}$ over a 10^6 Hz bandwidth, the power spectral density has to be $S_c(\omega) \approx 10^4 / (6\omega)$, in units of $(\text{V/m})^2 / (\text{rad.s}^{-1})$.

So far we have only considered quasi-static noise. The presence of some residual amount of high-frequency noise could possibly lead to errors while performing quantum operations. Below we discuss these high-frequency sources, finding that they will cause much smaller errors compared to quasi-static noise.

In general, a driven qubit Rabi-oscillates with a decay envelope function given by^{S19} $\zeta(t) \exp(-\Gamma_R t)$, where $\zeta(t)$ represents decay due to quasi-static detuning noise and Γ_R the exponential Rabi decay rate, which combines the qubit relaxation rate, Γ_1 , the inverse of the gate time jitter due to quasi-static noise, Γ_1^Δ , the inverse of the gate time jitter due to noise at the drive frequency, Γ_1^ν , (the last three yield $T_{2\rho}$ in the dressed qubit picture^{S20}) and the decay rate due to detuning noise at the Rabi frequency, Γ_Ω (which equals the inverse of $T_{1\rho}$ in the dressed qubit picture^{S20,S21}).

The effects of $\zeta(t)$, Γ_1 and Γ_1^Δ have already been discussed extensively in this manuscript, with corresponding error levels below 10^{-3} . We now focus on errors due to high-frequency noise sources, corresponding to decay rates Γ_1^ν and Γ_Ω .

Vertical (thus parallel to the driving field E_{ac}) noise at the qubit resonance frequency ($\sim 10^{10}$ Hz) would cause transitions between the qubit eigenstates – essentially a spurious excitation/relaxation process driven by noise – at a rate Γ_1^ν . During gate operations, the portion of the noise spectrum around the qubit fre-

quency adds incoherently to the external resonant drive, and causes the gate time to fluctuate. This noise can be caused *e.g.* by vertical dipoles fluctuating in resonance with the qubit or by voltage noise at the metallic gates. For the flip-flop qubit, the Rabi decay rate is given by $\Gamma_1^\nu = (\pi/2)(\mu_e^{\text{ff}}/\hbar)^2 S(2\pi\epsilon_{\text{ff}})$, where $\mu_e^{\text{ff}} = ed(g_{\text{so}}/\delta_{\text{so}})$ is the average flip-flop qubit electric dipole moment and $S(2\pi\epsilon_{\text{ff}})$ is the noise power spectral density at the qubit angular frequency (in units of $(\text{V/m})^2 / (\text{rad.s}^{-1})$). In case of charge noise, $S_c(\omega) = 10^4 / (6\omega)$, which gives $\Gamma_1^\nu \sim 10^4$ Hz. This implies $\pi/2$ x -gate errors $\sim 10^{-4}$. In case of Johnson-Nyquist noise, $S_{\text{JN}}(\omega) = 2 \times 10^{14} R \hbar \omega \pi^{-1} (e^{\hbar\omega/k_B T} - 1)^{-1}$ (where we have used $\partial E_z / \partial V = 10^7 \text{ m}^{-1}$, typical in MOS nanostructures). Because of the very low powers required by the electrically-driven 1-qubit gates ($< 1 \text{ pW}$), it is possible to insert abundant low-temperature attenuation along the high-frequency lines, insuring that the gates are well thermalized, and the noise of the room-temperature electronics greatly attenuated. A noise temperature $T = 100 \text{ mK}$ would give $\Gamma_1^\nu < 10^4$ Hz, and therefore error rates $< 10^{-4}$. Finally, in case of EWJN at $T = 100 \text{ mK}$, the 10^{10} Hz part of the spectrum is^{S18,S22} $S_{\text{EW}}(\omega) \approx \hbar\omega / (4\pi z^3 \sigma)$. This would give $\Gamma_1^\nu < 10^4$ Hz, therefore again error rates $< 10^{-4}$.

Noise at the Rabi frequency ($\Omega_R > 10^7$ Hz) causes decay in the Rabi oscillations at a rate Γ_Ω . This type of noise feeds into the driven qubit via fluctuations in the detuning between drive frequency and the qubit precession frequency. The decay rate of the flip-flop qubit is given by $\Gamma_\Omega = (\pi/2)(2\pi \sum_{i=x,y,z} \partial\epsilon_{\text{ff}}/\partial E_i)^2 S(\Omega_R)$. At the low-error operation region of Fig. 3f, $\partial\epsilon_{\text{ff}}/\partial E_z \sim 10^3 \text{ HzV}^{-1}\text{m}$ and $\partial\epsilon_{\text{ff}}/\partial E_{x,y} \sim 10^2 \text{ HzV}^{-1}\text{m}$ (from Fig. S2). $1/\nu$ charge noise gives $\Gamma_\Omega < 10^4$ Hz, implying $< 10^{-4}$ errors. Johnson-Nyquist noise from room temperature gives $\Gamma_\Omega = 3 \times 10^2$ Hz, whereas EWJN at 100 mK gives $\Gamma_\Omega = 2 \times 10^1$ Hz, therefore producing $< 10^{-5}$ and $< 10^{-6}$ errors, respectively.

We conclude that the sources of error treated in the main text, namely quasi-static E_z noise and charge-phonon relaxation, are the most deleterious ones for flip-flop qubits. Therefore our analysis is sufficient to provide a reliable estimate of dephasing and gate errors. Indeed, low-frequency noise was found to be the most deleterious one in a hybrid donor-dot qubit in a silicon MOS device^{S16}. Finally, note that we do not assume any type of dynamical noise correction or cancellation to be applied, and therefore our calculations are a worst-case scenario.

S4. Screening effect of metals and dielectrics

Our device topology consists of a SiO_2 layer sandwiched between a metal gate and silicon substrate, with the donor embedded in the substrate. In such a topology, the image charges of the donor electron and nucleus will be located above the donor, thereby creating an ad-

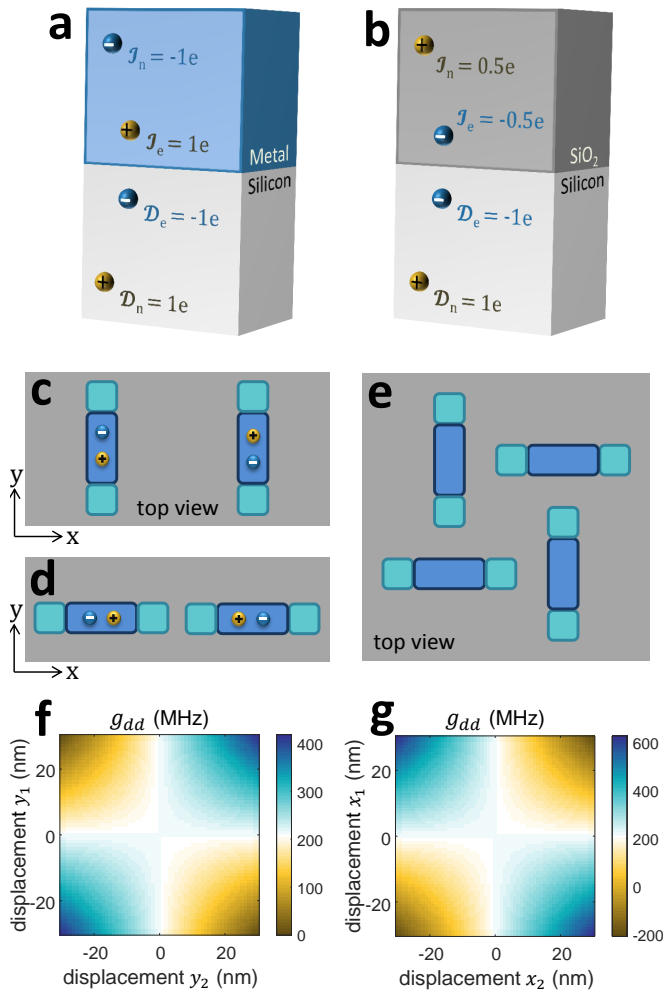


FIG. S3. **Screening and image charges.** Image (\mathcal{I}_e and \mathcal{I}_n) charges of the donor electron (\mathcal{D}_e) and nucleus (\mathcal{D}_n) for silicon-metal (a) and silicon-oxide (b) interfaces. The magnitude and polarity of the image charges are given by Eq. S1a. Schematic top view of two interacting dipoles when the negative charges (blue spheres) are displaced in perpendicular (c) and parallel (d) direction to the inter-dipole separation. e, Top view of gate stack that tunes each qubit's V_i by displacing their interface states perpendicularly to their nearest neighbor displacement, leaving g_{dd} unchanged. Inter-dipole coupling g_{dd} , as predicted by Eq. S3, for the orientation shown in c (f) and d (g), for $r = 200$ nm, $d_1 = d_2 = 10$ nm and $Q = -0.5$.

ditional vertical dipole. In this section, we quantify the variation of the dipolar coupling g_{dd} due to the electric field from the additional dipole, and arrive to the conclusion that g_{dd} will most likely be enhanced.

The magnitude and polarity of the image charges depend on the details of the nanostructure, such as the donor depth and thickness of the oxide. We first analyze two extreme scenarios considering image charges at (i) silicon-metal and (ii) silicon-oxide interfaces. For a source donor electron (or nuclear) charge $\mathcal{D}_{e(n)}$, in silicon, the image charge $\mathcal{I}_{e(n)}$ in the interface material is

given by^{S3}

$$\mathcal{I}_{e(n)} = Q \mathcal{D}_{e(n)}, \quad (\text{S1a})$$

$$Q = \frac{\epsilon_{\text{Si}} - \epsilon_{\text{I}}}{\epsilon_{\text{Si}} + \epsilon_{\text{I}}}, \quad (\text{S1b})$$

where $\epsilon_{\text{Si}} = 11.7$ is the dielectric constant of silicon, $\epsilon_{\text{I}} = 3.9$ and ∞ for oxide and metal interfaces respectively. Figures S3a,b show the magnitude and polarity of the image charges for both types of interfaces. For simplicity, we assume in Fig. S3 and Eq. S1a that the donor electron as well as its image are point charges. Given that the separation between the two donors is at least 180 nm (more than hundred times the Bohr radius of the donor electron), the above assumption is valid when calculating their dipolar interaction.

We first consider the electric dipole to be vertical. For the silicon-metal interface in Fig. S3a, $Q = -1$ and therefore the image charges have the opposite sign and same magnitude as the source charges. As a result, the total electric field E_{dip} from each donor will be enhanced by a factor of 2. This improves the electric dipole coupling g_{dd} between the two donors by a factor of 4. On the contrary, for the silicon-oxide interface in Fig. S3b, the image charges have the same sign and reduced magnitude ($Q = 0.5$) as the source charges, which decreases E_{dip} by half and therefore g_{dd} to a quarter of its bare value.

For a real device, which typically contains a few metal gates on top of a ~ 8 nm thick SiO_2 , it is difficult to make a precise estimate of the extra electric field from image charges. Rahman *et. al.*^{S3} assumed that a combination of metallic and oxide screening effects yields $Q = -0.5$, corresponding to an improvement in the magnitude of the electric dipole by $\approx 50\%$, which yields an improvement in g_{dd} by 125%. This means that, while building a real device, one would have to aim for slightly larger inter-donor separations than the ones presented in the main text.

Since the donor-interface tunnel coupling V_i has to be tuned to a precise value, the dipole will also have lateral components as shown on the insets of Fig. S2. These components will also be affected by image charges. In the case of a metallic interface, Fig. S3a, the lateral image dipole has opposite direction as the original one, and therefore the total lateral component will be completely screened. On the other hand, for the SiO_2 interface, Fig. S3b, the lateral component will be enhanced by 50%. Finally, for our assumed real structure ($Q = -0.5$), the lateral dipole will decrease to half its original value.

In more detail, the electric field of a donor-interface state will be the one produced by a dipole that includes both screening and angular effects,

$$\mathbf{D}_i = \mathbf{d}_i + Q \times (d_{i,x}, d_{i,y}, -d_{i,z}), \quad (\text{S2})$$

where \mathbf{d}_i refers to the bare dipole, with x , y and z components $d_{i,x}$, $d_{i,y}$ and $d_{i,z}$, respectively. We then modify the dipole-dipole interaction term, Eq. 15, to^{S23}:

$$g_{\text{dd}} = \frac{e^2}{16\pi\epsilon_0\epsilon_r\hbar} \frac{\mathbf{D}_1 \cdot \mathbf{D}_2 - 3(\mathbf{D}_1 \cdot \mathbf{r})(\mathbf{D}_2 \cdot \mathbf{r})/r^2}{r^3}, \quad (\text{S3})$$

which includes image charges and angular dependencies. Note that we neglect the interaction of a dipole with its own charge since it does not produce inter-donor coupling.

Laterally displacing the interface charge is, in general, necessary for the purpose of tuning the donor-interface tunnel coupling V_t . The same displacement, however, also alters the total electric dipole and can therefore affect the dipole-dipole coupling g_{dd} between neighboring qubits. We first consider the case in which the dis-

placements are perpendicular to the separation between dipoles, Fig. S3c. The g_{dd} dependence on y_1 and y_2 is plotted in Fig. S3f, for maximum displacements of 30 nm (enough to tune V_t by two orders of magnitude – see Fig S2). It shows that, provided that the interface states are displaced along the same direction, g_{dd} only varies by a factor of two. For completeness, we also analyze the case in which the interface states are displaced in the same direction as the inter-donor separation (Fig. S3d). As can be seen in the plot in Fig. S3g, g_{dd} varies by a factor of three if the interface states are displaced in opposite directions. Finally, the variation in g_{dd} can be reduced even further by fabricating the gate stack in such a way that the charges in neighboring qubits are displaced in perpendicular directions, as in Fig. S3e. In this way, from Eq. S3, the only dipole terms contributing to the coupling are the vertical ones, and therefore g_{dd} is unchanged (to first order) while tuning V_t .

-
- [S1] Kohn, W. & Luttinger, J. M. Theory of donor states in silicon. *Phys. Rev.* **98**, 915–922 (1955).
- [S2] Saraiva, A. L., Calderón, M. J., Hu, X., Das Sarma, S. & Koiller, B. Physical mechanisms of interface-mediated intervalley coupling in Si. *Phys. Rev. B* **80**, 081305 (2009).
- [S3] Rahman, R. *et al.* Orbital stark effect and quantum confinement transition of donors in silicon. *Phys. Rev. B* **80**, 165314 (2009).
- [S4] Calderón, M. J., Saraiva, A., Koiller, B. & Das Sarma, S. Quantum control and manipulation of donor electrons in Si-based quantum computing. *J. Appl. Phys.* **105**, 122410 (2009).
- [S5] Klimeck, G. *et al.* Atomistic simulation of realistically sized nanodevices using NEMO 3-D – part I: Models and benchmarks. *Electron Devices, IEEE Transactions on* **54**, 2079–2089 (2007).
- [S6] Klimeck, G. *et al.* Atomistic simulation of realistically sized nanodevices using NEMO 3-D – part II: Applications. *Electron Devices, IEEE Transactions on* **54**, 2090–2099 (2007).
- [S7] Yang, C. H., Rossi, A., Ruskov, R., Lai, N. S., Mohiyaddin, F. A., Lee, S., Tahan, C., Klimeck, G., Morello, A. & Dzurak, A. S. Spin-valley lifetimes in a silicon quantum dot with tunable valley splitting. *Nature Commun.* **4** (2013).
- [S8] Calderón, M. J., Koiller, B. & Das Sarma, S. Model of valley interference effects on a donor electron close to a Si/SiO₂ interface. *Phys. Rev. B* **77**, 155302 (2008).
- [S9] van Donkelaar, J. *et al.* Single atom devices by ion implantation. *J. Phys.: Condens. Matter* **27**, 154204 (2015).
- [S10] <http://www.synopsys.com/TOOLS/TCAD/>.
- [S11] Veldhorst, M. *et al.* An addressable quantum dot qubit with fault-tolerant control-fidelity. *Nature Nanotech.* **9**, 981–985 (2014).
- [S12] Kim, D. *et al.* High-fidelity resonant gating of a silicon-based quantum dot hybrid qubit. *npj Quantum Information* **1**, 15004 (2015).
- [S13] Thorgrimsson, B. *et al.* Mitigating the effects of charge noise and improving the coherence of a quantum dot hybrid qubit. *arXiv:1611.04945* (2016).
- [S14] Freeman, B. M., Schoenfeld, J. S., Jiang, H. Comparison of low frequency charge noise in identically patterned Si/SiO₂ and Si/SiGe quantum dots. *Appl. Phys. Lett.* **108**, 253108 (2016).
- [S15] Dial, O. E. *et al.* Charge noise spectroscopy using coherent exchange oscillations in a singlet-triplet qubit. *Phys. Rev. Lett.* **110**, 146804 (2013).
- [S16] Harvey-Collard, P. *et al.* Nuclear-driven electron spin rotations in a single donor coupled to a silicon quantum dot. *arXiv:1512.01606* (2015).
- [S17] Dehollain, J. P., Pla, J. J., Siew, E., Tan, K. Y., Dzurak, A. S. & Morello, A. Nanoscale broadband transmission lines for spin qubit control. *Nanotechnology* **24**, 015202 (2013).
- [S18] Henkel, C., Pötting, S. & Wilkens, M. Loss and heating of particles in small and noisy traps. *App. Phys. B* **69**, 379–387 (1999).
- [S19] Bylander, J. *et al.* Noise spectroscopy through dynamical decoupling with a superconducting flux qubit. *Nature Phys.* **7**, 565–570 (2011).
- [S20] Laucht, A. *et al.* A Dressed Spin Qubit in Silicon. *Nature Nanotechnol.* **12**, 61–66 (2017).
- [S21] Yan, F. *et al.* Rotating-frame relaxation as a noise spectrum analyser of a superconducting qubit undergoing driven evolution. *Nature Commun.* **4**, 2337 (2011).
- [S22] Poudel, A., Langsjoen, L. S., Vavilov, M. G. & Joynt, R. Relaxation in quantum dots due to evanescent-wave Johnson noise. *Phys. Rev. B* **87**, 045301 (2013).
- [S23] Ravets, S., Labuhn, H., Barredo, D., Beguin, L., Lahaye, T. & Browaeys, A. Coherent dipole-dipole coupling between two single Rydberg atoms at an electrically-tuned Rörster resonance. *Nature Phys.* **10**, 914–917 (2014).